Diffusion-RPO: Aligning Diffusion Models through Relative Preference Optimization

Yi $\mathrm{Gu}^{1,*}$, Zhendong $\mathrm{Wang}^{1,2,*}$, Yu
eqin Yin¹, Yujia Xie², and Mingyuan Zhou^{1,*}

{yigu, zhendong.wang, yueqin.yin}@utexas.edu, yujiaxie@microsoft.com, mingyuan.zhou@mccombs.utexas.edu

> ¹The University of Texas at Austin ²Microsoft Azure AI



Figure 1: Diffusion-RPO represents a novel approach that aligns Text-to-Image models with human preferences by optimizing diffusion model sampling steps and applying contrastive weighting to similar prompt-image pairs. As demonstrated by the samples above, the Diffusion-RPO fine-tuned SDXL-1.0 model successfully generates images that closely align with human preferences. The list of prompts is provided in the Appendix.

^{*}The first two authors contribute equally. *Corresponding Author.

Abstract

Aligning large language models with human preferences has emerged as a critical focus in language modeling research. Yet, integrating preference learning into Text-to-Image (T2I) generative models is still relatively uncharted territory. The Diffusion-DPO technique made initial strides by employing pairwise preference learning in diffusion models tailored for specific text prompts. We introduce Diffusion-RPO, a new method designed to align diffusion-based T2I models with human preferences more effectively. This approach leverages both prompt-image pairs with identical prompts and those with semantically related content across various modalities. Furthermore, we have developed a new evaluation metric, style alignment, aimed at overcoming the challenges of high costs, low reproducibility, and limited interpretability prevalent in current evaluations of human preference alignment. Our findings demonstrate that Diffusion-RPO outperforms established methods such as Supervised Fine-Tuning and Diffusion-DPO in tuning Stable Diffusion versions 1.5 and XL-1.0, achieving superior results in both automated evaluations of human preferences and style alignment. Our code is available at https://github.com/yigu1008/Diffusion-RPO

1 Introduction

Diffusion-based Text-to-Image (T2I) models have become the gold standard in image generative technologies. These models are typically pre-trained on extensive web datasets. However, this one-stage training approach may generate images that do not align with human preferences. In contrast, Large Language Models (LLMs) have seen significant advancements in producing outputs that cater to human preferences, primarily through a two-stage training process involving pre-training on web datasets followed by fine-tuning on preference data [Rafailov et al., 2023, Yin et al., 2024, Chen et al., 2024]. Extending this preference fine-tuning approach to T2I models [Wallace et al., 2024] presents opportunities to tailor image generation models to cater to diverse user preferences, enhancing their utility and relevance.

Recent research has concentrated on refining diffusion-based T2I models to better reflect human preferences, such as aesthetics and text-image alignment, through Reinforcement Learning from Human Feedback (RLHF) [Black et al., 2024, Clark et al., 2024, Fan et al., 2024, Lee et al., 2023, Prabhudesai et al., 2023, Xu et al., 2024]. This process typically involves pretraining a reward model to represent specific human preferences and then optimizing the diffusion models to maximize the reward of generated images. However, developing a robust reward model that accurately mirrors human preferences is challenging and computationally expensive. Over-optimizing the reward model often leads to significant issues of model collapse [Prabhudesai et al., 2023, Lee et al., 2023].

Diffusion-DPO [Wallace et al., 2024] incorporates Direct Preference Optimization (DPO) [Rafailov et al., 2023] into the preference learning framework of T2I diffusion models. DPO in LLMs focuses on contrasting chosen and rejected responses, bypassing the need for training additional reward models. However, DPO may not fully capture the nuances of human learning, which benefits from analyzing both successful examples and relevant failures [Dahlin et al., 2018].

Relative Preference Optimization (RPO) [Yin et al., 2024] proposes a learning method akin to human learning, where insights are derived from contrasting both identical and similar questions. RPO contrasts all chosen and rejected responses within a mini-batch, weighting each pair according to the similarity of their prompts. This contrastive preference learning approach has shown convincing improvements in aligning human preferences in LLMs compared to other baseline methods. Further discussions on related works can be found in Appendix B.

In this paper, we aim to adapt RPO for image preference learning in T2I diffusion models. By contrasting images generated from non-identical prompts, RPO can help the model discern overarching patterns in

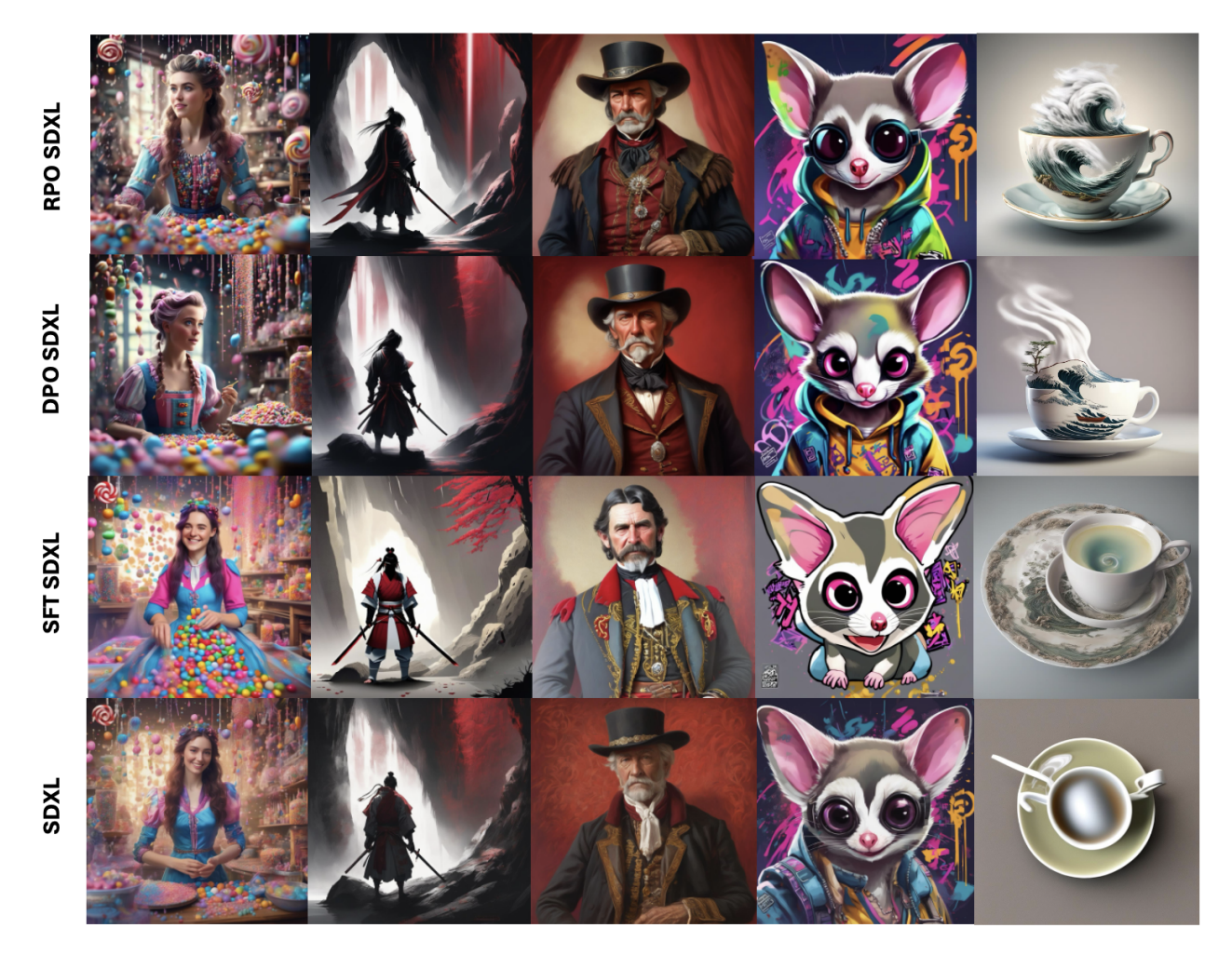


Figure 2: Sample images from RPO-SDXL The prompts used to generate the images are: "A whimsical candy maker in her enchanted workshop, surrounded by a cascade of multicolored candies falling like rain, wearing a bright, patchwork dress, her hair tinted with streaks of pink and blue, 8K, hyper-realistic, cinematic, post-production.", "A samurai cloaked in white with swords stands in a light beam of a dark cave, with a ruby red sorrow evident in the image.", "Victorian genre painting portrait of Royal Dano, an old west character in fantasy costume, against a red background.", and "A colorful anime painting of a sugar glider with a hiphop graffiti theme, by several artists, currently trending on Artstation.", "A typhoon in a tea cup, digital render"

color, lighting effects, and composition that align more closely with human preferences [Palmer et al., 2013]. However, adapting RPO to T2I diffusion models poses several significant challenges. Firstly, the log density of the final generated images is implicit and challenging to quantify in diffusion models because it involves integrating out all intermediate steps. Additionally, T2I diffusion models are inherently multi-modal, involving input prompts and output images in different modalities, which complicates the measurement of similarity between these multi-modal input-output pairs.

To overcome these challenges, we have 1) derived the RPO loss for diffusion models, simplifying it to apply relative preference alignment across each timestep, and 2) implemented the CLIP [Radford et al., 2021] encoder to project prompts and images into the same embedding space. This allows for the accurate measurement of similarity between multi-modal prompt-image pairs. Our experiments, as illustrated in Figure 2, validate our approach, demonstrating that learning preferences across non-identical prompts significantly enhances the alignment of generated images with human preferences in T2I models.

Moreover, our experiments highlight several shortcomings in the current evaluation metrics for human preference alignment. Traditional approaches like Diffusion-DPO rely on human evaluators, which not only incur substantial costs but also lead to results that are difficult to reproduce. While various reward models, such as HPSv2 [Wu et al., 2023], Pick Score [Kirstain et al., 2023], and ImageReward [Xu et al., 2024], have been pretrained on datasets labeled by humans to represent human preferences, the minimal variance in their reward scores often understates the differences in images as perceived by human preferences, complicating the assessment of whether a preference learning algorithm genuinely enhances alignment, as illustrated in Table 1.

To more effectively and reliably evaluate preference learning algorithms, we introduce a novel task called Style Alignment and have developed dedicated datasets for this purpose. This task aims to align the outputs of T2I models with specific styles, such as Van Gogh or sketch, identified as preferred samples within the dataset. We then measure the success of preference learning methods based on how closely the images generated by the fine-tuned model match these preferred styles.

We conduct empirical evaluations of Diffusion-RPO on state-of-the-art T2I models, including Stable Diffusion 1.5 [Rombach et al., 2022a] (SD1.5) and XL-1.0 [Podell et al., 2023b] (SDXL), and compare it with leading image preference alignment methods. Our experimental results show that Diffusion-RPO outperforms baseline methods in both human preference alignment and style alignment tasks by clear margins.

Our main contributions are summarized as follows:

- We adapt the RPO framework to diffusion-based T2I models, introducing a simplified step-wise denoising alignment loss and multi-modal re-weighting factors for improved effectiveness.
- We introduce Style Alignment, a new evaluation task for image preference learning that is less costly than using human labelers and yields more reproducible and interpretable results compared to traditional human preference reward models.
- Diffusion-RPO outperforms existing preference learning baselines across both automated evaluations of human preference and style alignment tasks.

2 Diffusion-RPO

In this section, we introduce Diffusion-RPO, a new diffusion-based preference learning algorithm that addresses the two challenges mentioned above. In LLM, $\pi_{\theta}(\boldsymbol{y} \mid \boldsymbol{x})$ is readily estimated through next-token prediction, given a specific response \boldsymbol{y} to a prompt \boldsymbol{x} . However, diffusion models approximate the probability of generating an image by reversing the forward diffusion process, $\pi_{\theta}(\boldsymbol{y}_{0:T} \mid \boldsymbol{x}) = \pi(\boldsymbol{y}_T) \prod_{t=T-1}^{t=1} \pi_{\theta}(\boldsymbol{y}_t | \boldsymbol{y}_{t+1}, \boldsymbol{x})$. To ease notation, we denote $\pi_{\theta}(\boldsymbol{y}_t | \boldsymbol{y}_{t+1}, \boldsymbol{x})$ as $\pi_{\theta}(\boldsymbol{y}_t | \boldsymbol{y}_{t+1})$ when there is no ambiguity. Integrating out all intermediate steps $\boldsymbol{y}_t \mid \boldsymbol{y}_{t+1}$ for all t < T is not feasible in practice due to the huge computational cost. Hence, we propose Diffusion-RPO and perform preference optimization at each diffusion reversing step. Following Ethayarajh et al. [2024] and Yin et al. [2024], we define the step-wise reward function for diffusion models as

$$r(\boldsymbol{y}_{t}^{w} \mid \boldsymbol{y}_{t+1}^{w}) = \beta \log \frac{\pi_{\theta}(\boldsymbol{y}_{t}^{w} \mid \boldsymbol{y}_{t+1}^{w})}{\pi_{\text{ref}}(\boldsymbol{y}_{t}^{w} \mid \boldsymbol{y}_{t+1}^{w})}$$
(1)

where β is the regularization hyper-parameter as in Wallace et al. [2024] and Rafailov et al. [2023]. Then, we define the RPO loss at each reverse diffusion step t as:

$$\mathcal{L}_{\text{Diffusion-RPO},t}(\theta) = \omega_{i,j} \log \sigma \left(\beta \log \frac{\pi_{\theta}(\boldsymbol{y}_{t,i}^{w} | \boldsymbol{y}_{t+1,i}^{w})}{\pi_{\text{ref}}(\boldsymbol{y}_{t,i}^{w} | \boldsymbol{y}_{t+1,i}^{w})} - \beta \log \frac{\pi_{\theta}(\boldsymbol{y}_{t,j}^{l} | \boldsymbol{y}_{t+1,j}^{l})}{\pi_{\text{ref}}(\boldsymbol{y}_{t,j}^{l} | \boldsymbol{y}_{t+1,j}^{l})} \right)$$
(2)

Note that different from Yin et al. [2024], the embedding distance weighting is performed outside the log-sigmoid function as we have observed superior empirical performance with this modified formulation.

Following DDPM [Ho et al., 2020], we then optimize the diffusion models across all timesteps t,

$$\tilde{\mathcal{L}}(\theta) = \mathbb{E}_{t \sim \mathcal{U}[1, T-1]} \left[\lambda(t) \cdot \omega_{i,j} \log \sigma \left(\beta \log \frac{\pi_{\theta}(\boldsymbol{y}_{t,i}^{w} | \boldsymbol{y}_{t+1,i}^{w})}{\pi_{\text{ref}}(\boldsymbol{y}_{t,i}^{w} | \boldsymbol{y}_{t+1,i}^{w})} - \beta \log \frac{\pi_{\theta}(\boldsymbol{y}_{t,j}^{l} | \boldsymbol{y}_{t+1,j}^{l})}{\pi_{\text{ref}}(\boldsymbol{y}_{t,j}^{l} | \boldsymbol{y}_{t+1,j}^{l})} \right) \right]$$
(3)

where t is uniformly sampled from [1, T-1], and $\lambda(t)$ is the timestep re-weighting factor. Similar to Ho et al. [2020], this re-weighting factor is chosen to be constant for all timesteps. In the following two sections, we will explore (a) how to define $\omega_{i,j}$ for multi-modal T2I tasks and (b) how to efficiently estimate $\pi_{\theta}(\boldsymbol{y}_t^l \mid \boldsymbol{y}_{t+1}^l)$ by using only $(\boldsymbol{y}_0^w, \boldsymbol{y}_0^l, \boldsymbol{x})$ from the offline dataset.

2.1 Contrastive Weights for Image Preference Learning

In RPO [Yin et al., 2024], we assign a weight $\omega_{i,j}$ to a pair of preference data, denoted as $(\boldsymbol{y}_i^w, \boldsymbol{x}_i^w)$ and $(\boldsymbol{y}_j^l, \boldsymbol{x}_j^l)$, by comparing their text embeddings. This weighting scheme utilizes the semantically related preference pairs within the batch and is the core to the success of RPO. In T2I models, we have multi-modal preference data with prompt and image. To this end, we introduce multi-modal distance weights that consider the context of both the prompt and image. This adaptation is designed to enhance the learning of preferences in T2I models by capturing the intricate interplay between textual and visual modalities.

Multi-Modal Embedding Distance Weights Denote (y, x), (y', x') as two image-prompt pairs and f(y, c) as an encoder that extracts image-text embeddings. The RPO distance weight is defined as

$$\tilde{\omega} = \exp(-\frac{\cos(f(\boldsymbol{y}, \boldsymbol{x}), f(\boldsymbol{y}', \boldsymbol{x}'))}{\tau})$$

where $\cos(f(\boldsymbol{y},\boldsymbol{x}),f(\boldsymbol{y}',\boldsymbol{x}'))=1-\frac{f(\boldsymbol{y},\boldsymbol{x})^Tf(\boldsymbol{y}',\boldsymbol{x}')}{||f(\boldsymbol{y},\boldsymbol{x})||_2||f(\boldsymbol{y}',\boldsymbol{x}')||_2}, \tau$ is the temperature parameter that determines the sensitivity of the weight against the change in embedding distance. Smaller τ leads to greater sensitivity to variations in embedding distance, resulting in weights that focus on pairs that are very close in terms of semantic meaning and visual appearance. Conversely, a higher τ leads to more uniform weight distribution.

In our setting with paired preference data: $\mathcal{D} = (\boldsymbol{y}^w, \boldsymbol{y}^l, \boldsymbol{x})$. Let M be the size of the minibatch. The unnormalized distance weight matrix $\tilde{\mathbf{W}} \in \mathbb{R}^{M \times M}$ is then defined as $\tilde{\mathbf{W}}_{i,j} = \tilde{\omega}_{i,j}$, where $\tilde{\omega}_{i,j} = \exp(-\frac{\cos(f(\boldsymbol{y}_i^w, \boldsymbol{x}_i^w), f(\boldsymbol{y}_j^l, \boldsymbol{x}_j^l))}{\tau})$. Following Yin et al. [2024], we normalize the distance weights on each row of the weight matrix so that the sum of each row of \mathbf{W} equals 1. Intuitively, the distance matrix measures the similarity between preference pairs $(\boldsymbol{y}_i^w, \boldsymbol{x}_i^w)$ and $(\boldsymbol{y}_j^l, \boldsymbol{x}_j^l), i, j \in [M]$. The diagonal elements corresponds to the preference pairs with identical prompt. The off-diagonal elements represent the contrast within the batch among preference pairs associated with different prompts. This approach leverages all available preference pairs within the batch and enhances image preference learning.

2.2 Sampling Diffusion Chain from Offline data

Given (y_0^w, y_0^l, x) , Diffsuion RPO loss in Equation (3) requires samples y_t, y_{t+1} to evaluate the log probability $\log \pi_{\theta}(y_t \mid y_{t+1})$. Note that y_t, y_{t+1} are dependent with respect to the same y_0 , and one can be efficiently derived from the forward process of Diffusion-based generative models [Ho et al., 2020]. The forward process is defined to gradually add Gaussian noise to the data $y_0 \sim q(y_0)$ according to a variance schedule β_1, \ldots, β_T :

$$q(\boldsymbol{y}_{1:T} \mid \boldsymbol{y}_0) := \prod_{t=1}^{T} q(\boldsymbol{y}_t \mid \boldsymbol{y}_{t-1}), \quad q(\boldsymbol{y}_t \mid \boldsymbol{y}_{t-1}) := \mathcal{N}\left(\boldsymbol{y}_t; \sqrt{1-\beta_t} \boldsymbol{y}_{t-1}, \beta_t \boldsymbol{I}\right)$$
(4)

Next, we introduce how we derive y_t , y_{t+1} and $\pi_{\theta}(y_t \mid y_{t+1})$.

Maginal Sampling The forward process admits sampling y_t at an arbitrary timestep t in closed form. Let $\alpha_t := 1 - \beta_t$ and $\bar{\alpha}_t := \prod_{s=1}^t \alpha_s$. With the re-parametrization trick, we have

$$\mathbf{y}_{t+1} = \sqrt{\bar{\alpha}_t} \mathbf{y}_0 + (1 - \bar{\alpha}_t) \boldsymbol{\epsilon}_{t+1}, \boldsymbol{\epsilon}_{t+1} \sim \mathcal{N}(\mathbf{0}, \mathbf{I})$$
 (5)

For $\forall t$, we directly sample y_{t+1} according to Equation (5) in the forward diffusion process.

Denoising with Ground Truth Following the usual practice [Ho et al., 2020, Xiao et al., 2021, Wang et al., 2023b, Zhou et al., 2023], we sample $y_t|y_{t+1}, y_0$ from the conditional posterior distribution of previous diffusion steps,

$$q(\mathbf{y}_{t} \mid \mathbf{y}_{t+1}, \mathbf{y}_{0}) = \mathcal{N}\left(\mathbf{y}_{t}; \tilde{\boldsymbol{\mu}}_{t+1}(\mathbf{y}_{t+1}, \mathbf{y}_{0}), \tilde{\beta}_{t+1}\mathbf{I}\right),$$
(6)

where $\tilde{\boldsymbol{\mu}}_{t+1}(\boldsymbol{y}_{t+1}, \boldsymbol{y}_0) := \frac{\sqrt{\bar{\alpha}_t}\beta_{t+1}}{1-\bar{\alpha}_{t+1}}\boldsymbol{y}_0 + \frac{\sqrt{\alpha_{t+1}}(1-\bar{\alpha}_t)}{1-\bar{\alpha}_{t+1}}\boldsymbol{y}_{t+1}$ and $\tilde{\beta}_{t+1} := \frac{1-\bar{\alpha}_t}{1-\bar{\alpha}_{t+1}}\beta_t$. Using the Gaussian reparametrization, and replacing the \boldsymbol{y}_0 with \boldsymbol{y}_{t+1} in Equation (5), we could obtain

$$\boldsymbol{y}_{t} = \sqrt{\frac{\alpha_{t}}{\alpha_{t+1}}}(\boldsymbol{y}_{t+1} - \frac{\beta_{t+1}}{\sqrt{1-\bar{\alpha}_{t+1}}}\boldsymbol{\epsilon}_{t+1}) + \sigma_{t+1}\boldsymbol{\epsilon}_{t}$$

where $\sigma_{t+1}^2 = \tilde{\beta}_{t+1} = \frac{1-\bar{\alpha}_{t1}}{1-\bar{\alpha}_{t+1}}\beta_{t+1}$, $\epsilon_t \sim \mathcal{N}\left(0, \boldsymbol{I}\right)$. Following the denoising model definition in DDPM [Ho et al., 2020], we parameterize $\pi_{\theta}(\boldsymbol{y}_t \mid \boldsymbol{y}_{t+1})$ as follows:

$$\pi_{\theta}(\boldsymbol{y}_{t} \mid \boldsymbol{y}_{t+1}) = \mathcal{N}(\boldsymbol{y}_{t}; \sqrt{\frac{\alpha_{t}}{\alpha_{t+1}}} (\boldsymbol{y}_{t+1} - \frac{\beta_{t+1}}{\sqrt{1 - \bar{\alpha}_{t+1}}} \boldsymbol{\epsilon}_{\theta}(\boldsymbol{y}_{t+1}, t+1)), \sigma_{t+1}^{2} \boldsymbol{I})$$
(7)

For simplicity, we approximate y_t with its posterior mean: $\mathbb{E}[y_t \mid y_{t+1}, y_0] = \sqrt{\frac{\alpha_t}{\alpha_{t+1}}} (y_{t+1} - \frac{\beta_{t+1}}{\sqrt{1-\bar{\alpha}_{t+1}}} \epsilon_{t+1})$. We then plug y_t and y_{t+1} into Equation (7), and derive

$$\pi_{\theta}(\boldsymbol{y}_{t}|\boldsymbol{y}_{t+1}) \approx \frac{1}{\left(\sqrt{2\pi\sigma_{t+1}^{2}}\right)^{d}} \exp\left(-\frac{1}{2} \frac{\beta_{t+1}}{(1-\bar{\alpha}_{t})} \frac{\alpha_{t}}{\alpha_{t+1}} \left\|\boldsymbol{\epsilon}_{\theta}(\boldsymbol{y}_{t+1}, t+1) - \boldsymbol{\epsilon}_{t+1}\right\|_{2}^{2}\right)$$
(8)

where d is the dimension of the image vector.

Note that $\pi_{\theta}(y_t|y_{t+1})$ follows the same formula for both preferred and rejected sample pairs. Combining Equations (3) and (8), with a constant timestep re-weighting [Ho et al., 2020, Wallace et al., 2024], yields our final Diffusion-RPO loss:

$$\mathcal{L}_{\text{Diffusion-RPO}}(\theta) = -\mathbb{E}\left[\omega_{i,j}\log\sigma\left(-\frac{1}{2}\beta(\left\|\boldsymbol{\epsilon}_{\theta}(\boldsymbol{y}_{t+1,i}^{w},t) - \boldsymbol{\epsilon}^{w}\right\|_{2}^{2} - \left\|\boldsymbol{\epsilon}_{\text{ref}}(\boldsymbol{y}_{t+1,i}^{w},t) - \boldsymbol{\epsilon}^{w}\right\|_{2}^{2} - \left(\left\|\boldsymbol{\epsilon}_{\theta}(\boldsymbol{y}_{t+1,j}^{l},t) - \boldsymbol{\epsilon}^{l}\right\|_{2}^{2} - \left\|\boldsymbol{\epsilon}_{\text{ref}}(\boldsymbol{y}_{t+1,j}^{l},t) - \boldsymbol{\epsilon}^{l}\right\|_{2}^{2}\right)\right)\right]$$

$$(9)$$

We provide the detailed derivation in Appendix A.

We notice a strong connection between the loss shown above with that of conditional transport [Zheng and Zhou, 2021, Tanwisuth et al., 2021], where ω_{ij} with $\sum_{j} \omega_{ij} = 1$ can be interpreted as the probability of transporting to the jth losing prompt-image pair $(\boldsymbol{x}_{j}, \boldsymbol{y}_{t+1,j}^{l})$ given the ith winning prompt-image pair $(\boldsymbol{x}_{i}, \boldsymbol{y}_{t+1,i}^{w})$ as the origin of the transport, while the (i,j) term transformed by $\log \sigma(\cdot)$ would be considered as the cost of transporting from $(\boldsymbol{x}_{i}, \boldsymbol{y}_{t+1,i}^{w})$ to $(\boldsymbol{x}_{j}, \boldsymbol{y}_{t+1,j}^{l})$. From the conditional transport perspective, for each winning pair $(\boldsymbol{x}_{i}, \boldsymbol{y}_{t+1,i}^{w})$, Diffusion-RPO computes the distance between the winning pair and all losing pairs in the mini-batch and prioritizes maximizing the cost from transporting from $(\boldsymbol{x}_{i}, \boldsymbol{y}_{t+1,i}^{w})$ to the losing pairs in CLIP latent space. This approach effectively minimizes the likelihood of sampling losing images that are semantically related to $(\boldsymbol{x}_{i}, \boldsymbol{y}_{t+1,i}^{w})$. This perspective may allow further improvement by adhering to the conditional-transport framework, yet modifying the definitions of transport probabilities and point-to-point transport cost to better serve the purpose of preference optimization. We leave this investigation to future study.

3 Style Alignment Dataset

The state-of-the-art evaluation metric for human preference learning on T2I models consists of two components:
(a) Human evaluation via employed labelers, (b) Automatic evaluation leveraging human preference reward models like HPSV2 [Wu et al., 2023] and Pick Score [Kirstain et al., 2023]. (1) Cost and Reproducibility in Human Evaluation: Diffusion-DPO [Wallace et al., 2024] evaluates employed labelers on Amazon Mechanical Turk to compare image generations which is costly and suffers from poor reproducibility due to the subjective nature of human preferences. (2) Difficulties in Automatic Evaluation: As suggested by Wallace et al. [2024], diffusion-based T2I models are pre-trained on datasets designed to align with human preferences. Consequently, Vanilla T2I models are inherently task-tuned towards human preference alignment. This scenario presents two significant challenges:

(a) Preference learning shows limited improvement in task-tuned models, a phenomenon also observed in the LLM summarization task by Rafailov et al. [2023]. (b) The performance of Supervised Fine-Tuning (SFT) varies depending on the capacity of the Vanilla model selected. Both the pre-training and fine-tuning data are collected to enhance alignment with human preferences, making the quality of the preference dataset pivotal to SFT performance. SFT can dramatically improve evaluation scores when the preference data is of higher quality than the model's generations. Conversely, it can degrade performance if the model was pre-trained on images of superior quality. This variability can undermine the effectiveness of automatic evaluations.

These issues highlight the complex interplay between model capacity and data quality of fine-tuning models that are already implicitly preference-tuned during pre-training.

To address the limitations inherent in current image preference evaluation metrics, we introduce a novel downstream task with datasets specifically designed for image preference learning, which we term **Style Alignment**. Style alignment aims to fine-tune T2I models to generate images that align with the offline data to achieve style transfer [Gatys et al., 2015, 2016] on T2I models. These styles are intentionally chosen to be visually distinct from those in the Pick-a-Pic V2 dataset, thereby enhancing the divergence between downstream tasks and pretraining. We constructed three datasets in Van Gogh, Sketch, and Winter styles each containing 10,000 preference pairs.

Preference Pair Construction The concept of style transfer is particularly well-suited to the field of image preference learning. We label the edited image after style transfer as preferred and the original image as rejected to fine-tune T2I models towards generating images with desired style. Our datasets are crafted based on subsets of Pick-a-Pic V2 [Kirstain et al., 2023]. For each pair of images in the subset, we randomly pick one as rejected and process it with state-of-the-art image editing models: Prompt Diffusion [Wang et al., 2023a] for Sketch and Winter style and Instruct Pix2Pix [Brooks et al., 2023] for Van Gogh style. The new image after style transfer is labeled as preferred. Notationally, the new datasets follow the same format as Pick-a-Pic V2: (y^w, y^l, x) , where y^w is the image after style transfer, y^l is the image from Pick-a-Pic.

Content-Safer Dataset Pick-a-Pic V2 is collected through webapp without safety checking. We observed substantial amount of inappropriate content when exploring the dataset. To foster a safe and ethical research environment, we manually deleted the inappropriate prompts when creating our style transfer datasets. We will release our datasets to the public soon.

4 Experiments

In our study, we conduct experiments designed to address the following research questions: (1) Can Diffusion-RPO enhance the T2I models' ability to generate images that better align with human preference? (2) How do preference learning methods perform when applied to style alignment tasks? (3) What are the key factors



Figure 3: Example Images from Pick-a-pic, Van Gogh, Sketch and Winter Datasets

that affect the performance of Diffusion-RPO? (4) Could style alignment effectively address the challenges encountered in aligning with human preferences in image preference learning evalutaions?

4.1 Experiment Setup

Models and Datasets Following Wallace et al. [2024], our human preference alignment experiments are conducted on the Pick-a-Pic V2 dataset [Kirstain et al., 2023]. We conduct style alignment experiments on our style alignment datasets (Van Gogh, Sketch, and Winter). The experiments are conducted on Stable Diffusion 1.5 (SD1.5) and Stable Diffusion XL (SDXL).

Evaluation For human preference alignment, we evaluated the Pick Score, HPSV2, LAION Aesthetics score [Schuhmann, 2022], CLIP [Radford et al., 2021], and ImageReward [Xu et al., 2024], using the HPSV2 benchmark test prompts [Wu et al., 2023] and Parti-Prompts [Yu et al., 2022]. With each reward model, we report both average scores and win rates between RPO and the baselines. For style alignment, we quantified model performance using the Fréchet Inception Distance (FID) [Heusel et al., 2017], which measures the difference between the preferred images in our training set and those generated from the training prompts by the fine-tuned T2I model.

Implementations We build Diffusion-RPO upon the codebase of Diffusion-DPO [Wallace et al., 2024]. We leverage the CLIP encoder [Radford et al., 2021] to compute multi-modal embeddings. For human preference alignment, we performed one-stage fine-tuning with 2000 optimization steps on both models for SFT and RPO. We directly use the checkpoints provided by Diffusion-DPO¹. For style alignment, we also conduct one-stage fine-tuning. Additionally, following Rafailov et al. [2023], we perform two-stage fine-tuning which is

 $^{^{1}} The \ checkpoints \ are \ downloaded \ from \ https://huggingface.co/mhdang/dpo-sd1.5-text2image-v1 \ and https://huggingface.co/mhdang/dpo-sdxl-text2image-v1$

Table 1: Reward model scores for Diffusion-RPO and existing alignment approaches using prompts from the HPSV2 and Parti-Prompt datasets. The temperature parameter is chosen to be 0.01 on SD1.5 and 0.5 on SDXL. SFT achieves highest scores on SD1.5 while deteriorates SDXL, this can be attributed to the image quality of pick-a-pic, a detailed discussion is provided in section 4.2.

Model	Test Dataset	Method	HPS	Pick Score	Aesthetics	CLIP	Image Reward
CD1 F	HPSV2	Base	26.931	20.948	5.554	0.345	0.083
		SFT	27.882	21.499	5.817	0.353	0.683
		DPO [Wallace et al., 2024]	27.233	21.396	5.679	0.352	0.296
		RPO (ours)	27.373	21.425	5.694	0.351	0.342
SD1.5	Parti-Prompt	Base	26.704	21.375	5.330	0.332	0.159
		SFT	27.402	21.681	5.534	0.339	0.561
		DPO [Wallace et al., 2024]	26.934	21.626	5.405	0.339	0.321
		RPO (ours)	27.046	21.663	5.432	0.340	0.392
	HPSV2	Base	27.900	22.694	6.135	0.375	0.808
		SFT	27.555	22.069	5.847	0.373	0.692
		DPO [Wallace et al., 2024]	28.082	23.159	6.139	0.383	1.049
SDXL		RPO (ours)	28.658	23.208	6.163	0.383	1.046
	Parti-Prompt	Base	27.721	22.562	5.766	0.357	0.668
		SFT	27.081	21.657	5.536	0.358	0.545
		DPO [Wallace et al., 2024]	27.637	22.894	5.806	0.370	1.032
		RPO (ours)	28.456	22.980	5.872	0.367	1.077

expected to be more effective due to the domain gap between the pre-training of T2I models and the style alignment task. The details on learning rate and optimization steps are listed in Table 5.

4.2 Human Preference Alignment

Table 1 reports reward model scores for Diffusion-RPO, Diffusion-DPO [Wallace et al., 2024], SFT, and Base Stable Diffusion. On SDXL, Diffusion-RPO achieves better performance on all reward models comparing to the baselines except for slightly lower CLIP score on Parti-Prompt dataset. In particular, Diffusion-RPO achieves 28.658 HPSV2 score and 23.208 Pick Score on the HPSV2 benchmark dataset. On SD1.5, We observe that Diffusion-RPO outperforms Diffusion-DPO on HPSV2, PickScore, Aesthtics, and Image Reward. However, it is observed that SFT improves human preference alignment greatly on SD 1.5, achieving comparable result to Diffusion-RPO. We partially attribute this to the much higher quality of Pick-a-Pic generation (from SDXL-beta and Dreamlike) vs. Vanilla SD1.5, which is mentioned in Wallace et al. [2024]. Nevertheless, Diffusion-RPO outperforms Diffusion-DPO on four out of five metrics, achieving higher scores, though it scores slightly lower on the CLIP metric. The consistent improvement comparing to Diffusion-DPO [Wallace et al., 2024] in aligning SD1.5 and SDXL showcases that utilizing information from related prompt-image pairs would benefit image preference learning. Additionally, we observe that SFT-SDXL deteriorates SDXL performance. This could again be attributed to lower Pick-a-Pic generation quality comparing to SDXL-1.0.

Figure 2 provides a visual comparison of RPO-SDXL, DPO-SDXL, SFT-SDXL, and Base SDXL generations. In general Diffusion-RPO generates images with better quality. In the first example: "A whimsical candy maker in her enchanted workshop, surrounded by a cascade of multicolored candies falling like rain, wearing a bright, patchwork dress, her hair tinted with streaks of pink and blue, 8K, hyper-realistic, cinematic, post-production.", Diffusion-RPO generation depicts a candy shop which is illuminated with vibrant and visually appealing light, highlighting the colorful details and textures of the scene. This kind of lighting creates a lively, enchanting atmosphere. In the fourth Prompt: "A colorful anime painting of a sugar glider with a hiphop graffiti theme, by several artists, currently trending on Artstation.", Diffusion-RPO generates a more colorful sugar glider, which better aligns with the prompt. These examples showcase that Diffusion-RPO is able to generate images with finer details, better lighting effects, vivid colors and higher fidelity to the

Table 2: Comparison of the FID scores for images generated from training prompts using style-aligned T2I models, with the training images serving as references.

Method		SD1.5		SDXL		
	Van Gogh	Sketch	Winter	Van Gogh	Sketch	Winter
SFT	15.34	20.56	16.31	28.15	16.41	21.74
DPO [Wallace et al., 2024]	91.8	34.67	63.43	152.35	137.07	99.37
RPO (Ours)	42.24	29.36	33.29	97.57	59.75	85.54
SFT+SFT	14.73	19.89	16.06	22.71	30.48	30.78
SFT+DPO [Wallace et al., 2024]	47.47	24.92	26.26	25.62	23.32	20.02
SFT+RPO (Ours)	13.25	17.54	14.50	17.95	15.96	15.75

prompt. More examples from RPO-SDXL can be found in Appendix G.

4.3 Style Alignment

We report the FID between style-transferred images in the training data and the images generated by the finetuned models generated using the same training prompts. The results are provided in Table 2.

We observe that for one-stage fine-tuning, SFT is most effective in fine-tuning Vanilla T2I models due to the domain gap between vanilla Stable Diffusion Models and the style alignment dataset. Still, we observe that Diffusion-RPO better aligns the model to the desired style. In two-stage fine-tuning, Diffusion-RPO demonstrates superior performance for all 3 styles and 2 models. The outstanding performance of Diffusion-RPO is attributable to its ability of learning from all comparisons within the mini-batch. The less related prompts-image pairs could still benefit preference learning by the contrast in overall style and backgrounds.

Figure 4 showcases the performance of two-tage style alignment fine-tuning on SD1.5 and SDXL. The terms SFT, DPO, and RPO atop the image refer to performing SFT, Diffusion-DPO or Diffusion-RPO on SFT tuned models. We observe that on all three datasets, Diffusion-RPO successfully learns both details and the overall style, generating images that account for both style characteristics and fine details. we note that Diffusion-DPO tends to learn an incorrect style on the Van Gogh dataset, adding excessive green in the background. On the Winter dataset, Diffusion-DPO tends to over-emphasize the background and obscure the main body's details with snowflakes. Diffusion-DPO encounters similar issues on the Sketch dataset by generating a background that does not resemble a pencil-style sketch and obscures the details with black blocks. SFT can effectively learn the details but appears to be weaker in leaning the styles, especially in the background. We partially attribute the advantage of Diffusion-RPO over Diffusion-DPO and SFT to the use of related prompt-image pairs. By learning all the pairs in the mini-batch, Diffusion-RPO is able to capture the styles and composition more accurately, producing better quality images comparing to the baselines. More examples from style aligned Stable Diffusion models can be found in Appendix H.

4.4 Ablation Studies

We conducted ablation study on the distance temperature parameter τ with the aim of understanding how much the focus should we put on semantically related prompt-image pairs to enhance preference alignment. In our experiment, we compare the performance of Diffusion-RPO under different distance temperatures in both human preference alignment and style alignment. In Table 3, we report reward model scores from automatic evaluations and FID for style alignment. We find that a lower distance temperature (τ =0.01) leads to overall best performance being highest on HPS [Wu et al., 2023], Image Reward [Xu et al., 2024] and second highest on Pick Score [Kirstain et al., 2023]. On the style alignment task, it is observed that the style alignment

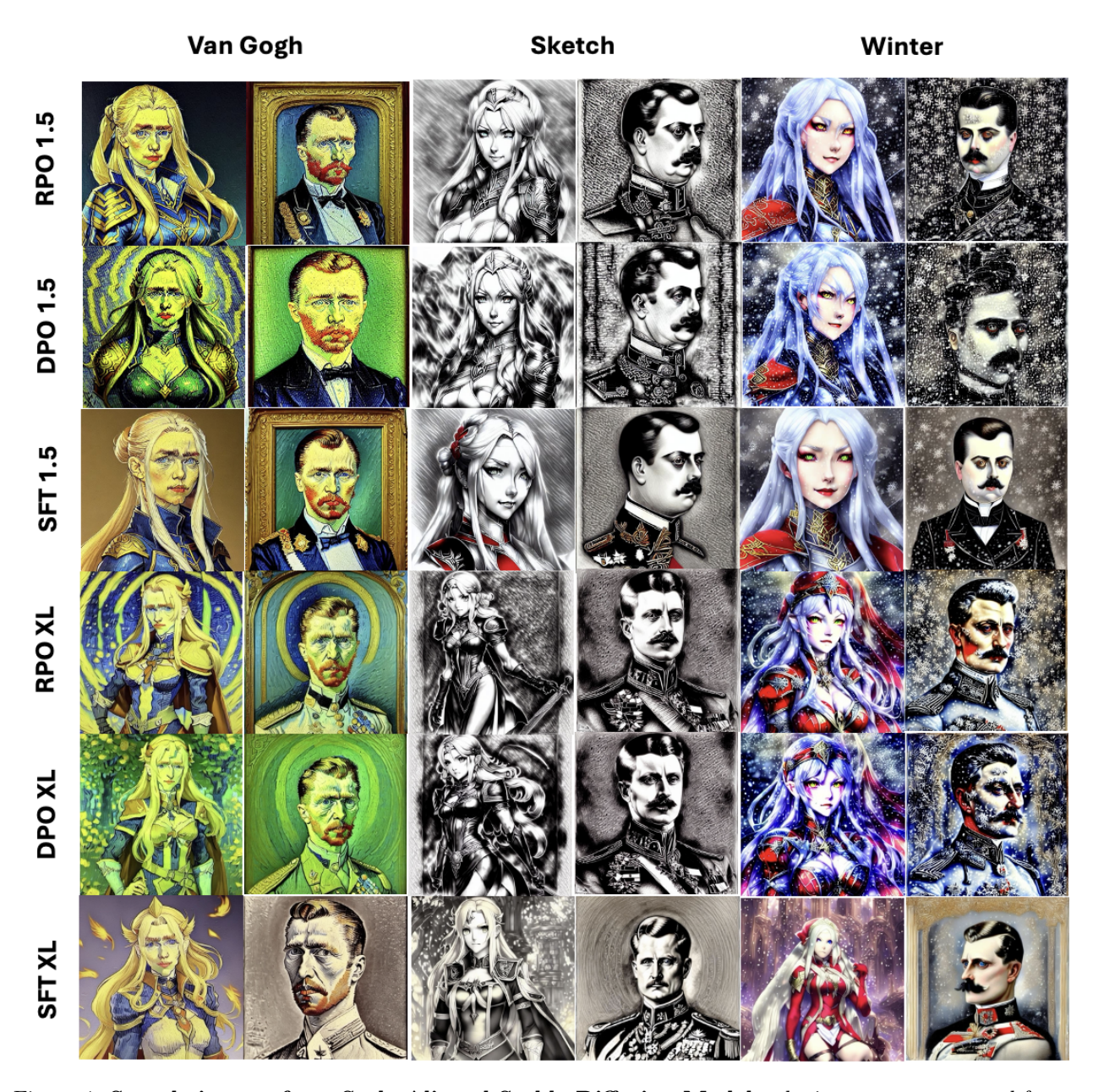


Figure 4: Sample images from Style Aligned Stable Diffusion Models, the images are generated from prompts: "Edelgard from Fire Emblem depicted in Artgerm's style.", "Portrait of Archduke Franz Ferdinand by Charlotte Grimm, depicting his detailed face."

performance improves as we increase the temperature. This contrast between human preference alignment and style alignment can be attributed to the differing natures of the two tasks: In human preference alignment tasks, a lower temperature focuses more on related prompt-image pairs to improve prompt-specific details. In style alignment tasks, however, correctly learning the overall image style becomes a major challenge. This is tackled by a higher temperature that results in more uniform weights for all preference pairs since any preference pair entails characteristics of image style that contributes to the alignment of styles.

Table 3: Ablation Study on Diffusion-RPO Temperature Parameters. We use SD1.5 as the base model for Huamn preference alginment and SFT-tuned SD1.5 for Van Gogh Style alignment. We reported reward model scores on HPSV2 test prompts and style alignment FID under various temperatures.

Temperature Parameter (τ)	0.01	0.1	1.0	2.0	5.0
HPS	27.373	27.286	27.245	27.176	27.205
Pick Score	21.425	21.448	21.417	21.366	21.421
Aesthetics	5.694	5.696	5.671	5.733	5.657
CLIP	0.351	0.352	0.353	0.353	0.352
Image Reward	0.342	0.335	0.320	0.270	0.316
Style Alignment FID	31.96	16.26	13.66	13.82	13.25

5 Conclusion

We introduce Diffusion-RPO as a novel method for aligning Text-to-Image (T2I) Models with human preferences. This approach enhances each sampling step of diffusion models and utilizes similar prompt-image pairs through contrastive weighting. On Stable Diffusion versions 1.5 and XL, Diffusion-RPO exhibited superior performance compared to previous alignment methods in both human preference alignment and our newly introduced style alignment tasks. The empirical findings highlight the effectiveness of Diffusion-RPO in fine-tuning diffusion-based T2I models and demonstrate the value of style alignment as a reliable measure for assessing image preference learning methods.

Limitations & Future Work Although Diffusion-RPO enhances the alignment of text-to-image models, it relies on a dataset collected from the web, which may not fully capture the diverse spectrum of human preferences across different communities. A potential avenue for future research could involve developing methods to collect datasets that reflect a wider range of cultural diversity. This would help in creating models that are more universally applicable and sensitive to various cultural nuances.

References

Hierarchical Text-Conditional Image Generation with CLIP Latents, April 2022. URL http://arxiv.org/abs/2204.06125. arXiv:2204.06125 [cs].

Kevin Black, Michael Janner, Yilun Du, Ilya Kostrikov, and Sergey Levine. Training diffusion models with reinforcement learning. In *International Conference on Learning Representations*, 2024.

Tim Brooks, Aleksander Holynski, and Alexei A. Efros. Instructpix2pix: Learning to follow image editing instructions. In *Proceedings of the IEEE/CVF Conference on Computer Vision and Pattern Recognition*. IEEE Computer Society, 2023.

Zixiang Chen, Yihe Deng, Huizhuo Yuan, Kaixuan Ji, and Quanquan Gu. Self-play fine-tuning converts weak language models to strong language models, 2024. URL https://arxiv.org/abs/2403.07691. Unpublished manuscript.

Kevin Clark, Paul Vicol, Kevin Swersky, and David J. Fleet. Directly fine-tuning diffusion models on differentiable rewards. In *Proceedings of the 11th International Conference on Learning Representations (ICLR 2024)*, 2024.

Kristina B Dahlin, You-Ta Chuang, and Thomas J Roulet. Opportunity, motivation, and ability to learn from failures and errors: Review, synthesis, and ways to move forward. *Academy of Management Annals*, Add volume number if available:252–277, 2018.

- Prafulla Dhariwal and Alex Nichol. Diffusion models beat gans on image synthesis. In *Advances in Neural Information Processing Systems*, volume 34, pages pages-if-known, 2021. doi: 10.48550/arXiv.2105.05233. URL https://arxiv.org/abs/2105.05233. Code available at https://github.com/openai/guided-diffusion.
- Kawin Ethayarajh, Winnie Xu, Niklas Muennighoff, Dan Jurafsky, and Douwe Kiela. Kto: Model alignment as prospect theoretic optimization. In *Proceedings of the International Conference on Machine Learning (ICML)*. ICML, 2024.
- Y. Fan, O. Watkins, Y. Du, H. Liu, M. Ryu, C. Boutilier, P. Abbeel, M. Ghavamzadeh, K. Lee, and K. Lee. Reinforcement learning for fine-tuning text-to-image diffusion models. In *Advances in Neural Information Processing Systems*, volume 36, page Refer to specific pages or omit if unknown, 2024.
- Leon A. Gatys, Alexander S. Ecker, and Matthias Bethge. A neural algorithm of artistic style. *The Journal Name*, Vol Number(Issue Number):Page Range, 2015.
- Leon A. Gatys, Alexander S. Ecker, and Matthias Bethge. Image style transfer using convolutional neural networks. In *Proceedings of the IEEE Conference on Computer Vision and Pattern Recognition (CVPR)*. IEEE, 2016.
- Martin Heusel, Hubert Ramsauer, Thomas Unterthiner, Bernhard Nessler, and Sepp Hochreiter. Gans trained by a two time-scale update rule converge to a local nash equilibrium. In *Advances in Neural Information Processing Systems*. NeurIPS, 2017.
- Jonathan Ho, Ajay Jain, and Pieter Abbeel. Denoising diffusion probabilistic models. In *Advances in Neural Information Processing Systems*. Curran Associates, Inc., 2020.
- Jiwoo Hong, Noah Lee, and James Thorne. Orpo: Monolithic preference optimization without reference model, 2024. URL https://arxiv.org/abs/2403.07691.
- Yuval Kirstain, Adam Polyak, Uriel Singer, Shahbuland Matiana, Joe Penna, and Omer Levy. Pick-a-pic: An open dataset of user preferences for text-to-image generation. In *Proceedings of the 37th Conference on Neural Information Processing Systems (NeurIPS 2023)*, 2023.
- K. Lee, H. Liu, M. Ryu, O. Watkins, Y. Du, C. Boutilier, P. Abbeel, M. Ghavamzadeh, and S.S. Gu. Aligning text-to-image models using human feedback. arXiv preprint arXiv:2302.12192, 2023.
- Ilya Loshchilov and Frank Hutter. Decoupled weight decay regularization. In *International Conference on Learning Representations*, Freiburg, Germany, 2019. ICLR.
- Alexander Quinn Nichol, Prafulla Dhariwal, Aditya Ramesh, Pranav Shyam, Pamela Mishkin, Bob McGrew, Ilya Sutskever, and Mark Chen. Glide: Towards photorealistic image generation and editing with text-guided diffusion models. In *International Conference on Machine Learning*, pages 16784–16804. PMLR, 2022.
- Stephen E. Palmer, Karen B. Schloss, and Jonathan Sammartino. Visual aesthetics and human preference. *Annual Review of Psychology*, 64:77–107, 2013. doi: 10.1146/annurev-psych-120710-100504. URL https://doi.org/10.1146/annurev-psych-120710-100504. First published as a Review in Advance on September 27, 2012.
- Dustin Podell, Zion English, Kyle Lacey, Andreas Blattmann, Tim Dockhorn, Jonas Müller, Joe Penna, and Robin Rombach. SDXL: Improving latent diffusion models for high-resolution image synthesis. arXiv:2307.01952 [cs], July 2023a. URL https://arxiv.org/abs/2307.01952. Available online at https://github.com/Stability-AI/generative-models.
- Dustin Podell, Zion English, Kyle Lacey, Andreas Blattmann, Tim Dockhorn, Jonas Müller, Joe Penna, and Robin Rombach. SDXL: Improving Latent Diffusion Models for High-Resolution Image Synthesis, July 2023b. URL http://arxiv.org/abs/2307.01952. arXiv:2307.01952 [cs].
- M. Prabhudesai, A. Goyal, D. Pathak, and K. Fragkiadaki. Aligning text-to-image diffusion models with reward backpropagation. arXiv preprint arXiv:2310.03739, 2023.

- Alec Radford, Jong Wook Kim, Chris Hallacy, Aditya Ramesh, Gabriel Goh, Sandhini Agarwal, Girish Sastry, Amanda Askell, Pamela Mishkin, Jack Clark, Gretchen Krueger, and Ilya Sutskever. Learning transferable visual models from natural language supervision. arXiv preprint, 2021.
- Rafael Rafailov, Archit Sharma, Eric Mitchell, Stefano Ermon, Christopher D. Manning, and Chelsea Finn. Direct preference optimization: Your language model is secretly a reward model. In *Advances in Neural Information Processing Systems*, 2023.
- Robin Rombach, Andreas Blattmann, Dominik Lorenz, Patrick Esser, and Björn Ommer. High-resolution image synthesis with latent diffusion models. In *Proceedings of the IEEE/CVF Conference on Computer Vision and Pattern Recognition*. IEEE/CVF, April 2022a. doi: 10.48550/arXiv.2112.10752. URL https://arxiv.org/abs/2112.10752.
- Robin Rombach, Andreas Blattmann, Dominik Lorenz, Patrick Esser, and Björn Ommer. High-Resolution Image Synthesis with Latent Diffusion Models, April 2022b. URL http://arxiv.org/abs/2112.10752. arXiv:2112.10752 [cs].
- Chitwan Saharia, William Chan, Saurabh Saxena, Lala Li, Jay Whang, Emily Denton, Seyed Kamyar Seyed Ghasemipour, Burcu Karagol Ayan, S. Sara Mahdavi, Rapha Gontijo Lopes, Tim Salimans, Jonathan Ho, David J. Fleet, and Mohammad Norouzi. Photorealistic text-to-image diffusion models with deep language understanding. In *Advances in Neural Information Processing Systems*, Virtual, December 2022. Neural Information Processing Systems Foundation. doi: 10.48550/arXiv.2205.11487. URL https://arxiv.org/abs/2205.11487. Code available at https://imagen.research.google/.
- C. Schuhmann. Laion-aesthetics. https://laion.ai/blog/laion-aesthetics/, 2022. Accessed: 2024-05-10.
- Noam Shazeer and Mitchell Stern. Adafactor: Adaptive learning rates with sublinear memory cost. In *Proceedings of the 35th International Conference on Machine Learning*. ICML, 2018.
- Jascha Sohl-Dickstein, Eric Weiss, Niru Maheswaranathan, and Surya Ganguli. Deep unsupervised learning using nonequilibrium thermodynamics. In *Proceedings of the 32nd International Conference on Machine Learning (ICML)*, pages 2256–2265. PMLR, 2015.
- Yang Song, Jascha Sohl-Dickstein, Diederik P Kingma, Abhishek Kumar, Stefano Ermon, and Ben Poole. Score-based generative modeling through stochastic differential equations. arXiv preprint arXiv:2011.13456, 2020.
- Korawat Tanwisuth, Xinjie Fan, Huangjie Zheng, Shujian Zhang, Hao Zhang, Bo Chen, and Mingyuan Zhou. A prototype-oriented framework for unsupervised domain adaptation. *Advances in Neural Information Processing Systems*, 34:17194–17208, 2021.
- Bram Wallace, Senthil Purushwalkam, Meihua Dang, Rafael Rafailov, Stefano Ermon, Linqi Zhou, Caiming Xiong, Aaron Lou, Nikhil Naik, and Shafiq Joty. Diffusion model alignment using direct preference optimization. arXiv preprint, 2024.
- Zhendong Wang, Yifan Jiang, Yadong Lu, Yelong Shen, Pengcheng He, Weizhu Chen, Zhangyang Wang, and Mingyuan Zhou. In-context learning unlocked for diffusion models. In *Advances in Neural Information Processing Systems*. NeurIPS, 2023a. The authors are affiliated with The University of Texas at Austin and Microsoft Azure AI.
- Zhendong Wang, Huangjie Zheng, Pengcheng He, Weizhu Chen, and Mingyuan Zhou. Diffusion-gan: Training gans with diffusion. In *International Conference on Learning Representations*. International Conference on Learning Representations, August 2023b. doi: 10.48550/arXiv.2206.02262. URL https://arxiv.org/abs/2206.02262. Project homepage: https://github.com/Zhendong-Wang/Diffusion-GAN.
- Xiaoshi Wu, Yiming Hao, Keqiang Sun, Yixiong Chen, Feng Zhu, Rui Zhao, and Hongsheng Li. Human preference score v2: A solid benchmark for evaluating human preferences of text-to-image synthesis. arXiv preprint, 2023. The authors are affiliated with Multimedia Laboratory, The Chinese University of Hong Kong, CUHK-SZ, SRIBD, SenseTime Research, Qing Yuan Research Institute, Shanghai Jiao Tong University, and Centre for Perceptual and Interactive Intelligence (CPII).

- Zhisheng Xiao, Karsten Kreis, and Arash Vahdat. Tackling the generative learning trilemma with denoising diffusion gans. arXiv preprint arXiv:2112.07804, 2021.
- J. Xu, X. Liu, Y. Wu, Y. Tong, Q. Li, M. Ding, J. Tang, and Y. Dong. Imagere-ward: Learning and evaluating human preferences for text-to-image generation. In Advances in Neural Information Processing Systems, volume 36, pages 2, 5, 10, 2024.
- Yueqin Yin, Zhendong Wang, Yi Gu, Hai Huang, Weizhu Chen, and Mingyuan Zhou. Relative preference optimization: Enhancing llm alignment through contrasting responses across identical and diverse prompts. arXiv preprint, 2024.
- Jiahui Yu, Yuanzhong Xu, Jing Yu Koh, Thang Luong, Gunjan Baid, Zirui Wang, Vijay Vasudevan, Alexander Kut, Yinfeng Yang, Burcu Karagol Ayan, et al. Scaling autoregressive models for content-rich text-to-image generation. Transactions on Machine Learning Research, 11, 11 2022. Available at OpenReview: https://openreview.net/forum?id=AFDcYJKhND.
- Huangjie Zheng and Mingyuan Zhou. Exploiting chain rule and Bayes' theorem to compare probability distributions. Advances in Neural Information Processing Systems, 34:14993–15006, 2021.
- Mingyuan Zhou, Tianqi Chen, Zhendong Wang, and Huangjie Zheng. Beta diffusion. In *Neural Information Processing Systems*, 2023. URL https://arxiv.org/abs/2309.07867.

A Mathematical Derivation

In this section we provide the details on the derivation of our Diffusion-RPO loss in Equation (9), we start from the loss function in Equation (3):

$$\mathcal{L}_{\text{Diffusion-RPO},t}(\theta) = \omega_{i,j} \log \sigma \left(\beta \log \frac{\pi_{\theta}(\boldsymbol{y}_{t}^{w} \mid \boldsymbol{y}_{t+1}^{w})}{\pi_{\text{ref}}(\boldsymbol{y}_{t}^{w} \mid \boldsymbol{y}_{t+1}^{w})} - \beta \log \frac{\pi_{\theta}(\boldsymbol{y}_{t}^{l} \mid \boldsymbol{y}_{t+1}^{l})}{\pi_{\text{ref}}(\boldsymbol{y}_{t}^{l} \mid \boldsymbol{y}_{t+1}^{l})} \right)$$
(10)

following Ho et al. [2020], the policies are of form:

$$\begin{split} \pi_{\theta}(\boldsymbol{y}_{t}^{*} \mid \boldsymbol{y}_{t+1}^{*}) &= \mathcal{N}\left(\boldsymbol{y}_{t}^{*}; \frac{\sqrt{\alpha_{t}}}{\sqrt{\alpha_{t+1}}}(\boldsymbol{y}_{t}^{*} - \frac{\beta_{t+1}}{\sqrt{1 - \bar{\alpha}_{t+1}}}\boldsymbol{\epsilon}_{\theta}(\boldsymbol{y}_{t+1}^{*}, t)), \sigma_{t+1}^{2} \boldsymbol{I}\right) \\ &= \frac{1}{\left(\sqrt{2\pi\sigma_{t+1}^{2}}\right)^{d}} \exp\left(-\frac{1}{2\sigma_{t+1}^{2}} \left\|\boldsymbol{y}_{t}^{*} - \sqrt{\frac{\alpha_{t}}{\alpha_{t+1}}}(\boldsymbol{y}_{t+1}^{*} - \frac{\beta_{t+1}}{\sqrt{1 - \bar{\alpha}_{t+1}}}\boldsymbol{\epsilon}_{\theta}(\boldsymbol{y}_{t+1}^{*}, t+1))\right\|_{2}^{2}\right) \end{split}$$

where d is the dimension of the image vector, we use \mathbf{y}_t^* for ease of notation. The derivation using \mathbf{y}_t^* is applicable to both $\mathbf{y}^w t, i$ and $\mathbf{y}^l t, j$.

The ground-truth denoising distribution and posterior mean can be written in the form:

$$q\left(\boldsymbol{y}_{t}^{*}\mid\boldsymbol{y}_{t}^{*},\boldsymbol{y}_{0}^{*}\right) = \mathcal{N}(\boldsymbol{y}_{t}^{*};\sqrt{\frac{\alpha_{t}}{\alpha_{t+1}}}(\boldsymbol{y}_{t}^{*} - \frac{\beta_{t+1}}{\sqrt{1-\bar{\alpha}_{t+1}}}\boldsymbol{\epsilon}_{t+1}),\sigma_{t+1}^{2}\boldsymbol{I})$$

$$= \frac{1}{\left(\sqrt{2\pi\sigma_{t+1}^{2}}\right)^{d}}\exp\left(-\frac{1}{2\sigma_{t+1}^{2}}\left\|\boldsymbol{y}_{t+1}^{*} - \sqrt{\frac{\alpha_{t}}{\alpha_{t+1}}}(\boldsymbol{y}_{t+1}^{*} - \frac{\beta_{t+1}}{\sqrt{1-\bar{\alpha}_{t+1}}}\boldsymbol{\epsilon}_{t+1})\right\|_{2}^{2}\right)$$

$$\mathbb{E}\left[\boldsymbol{y}_{t}^{*}\mid\boldsymbol{y}_{t+1}^{*},\boldsymbol{y}_{0}^{*}\right] = \sqrt{\frac{\alpha_{t}}{\alpha_{t+1}}}(\boldsymbol{y}_{t+1}^{*} - \frac{\beta_{t+1}}{\sqrt{1-\bar{\alpha}_{t+1}}}\boldsymbol{\epsilon}_{t+1})$$

where y_0^* is from the offline data \mathcal{D} , y_{t+1}^* is sampled from the forward process $q(y_{t+1}^* \mid y_0^*)$

If we sample \boldsymbol{y}_{t}^{*} from $q\left(\boldsymbol{y}_{t}^{*} \mid \boldsymbol{y}_{t+1}^{*}, \boldsymbol{y}_{0}^{*}\right)$, we can express $\boldsymbol{y}_{t}^{*} = \sqrt{\frac{\alpha_{t}}{\alpha_{t+1}}}(\boldsymbol{y}_{t+1}^{*} - \frac{\beta_{t+1}}{\sqrt{1-\bar{\alpha}_{t+1}}}\boldsymbol{\epsilon}_{t+1}) + \sigma_{t+1}\boldsymbol{\epsilon}_{t}$, where $\boldsymbol{\epsilon}_{t+1}$ is the noise added in the forward process to obtain \boldsymbol{y}_{t+1}^{*} , $\boldsymbol{\epsilon}_{t}$ is the Gaussian noise to obtain \boldsymbol{y}_{t}^{*} in the reverse process with the re-parametrization trick. The policy is then evaluated as:

$$\pi_{\theta}(\boldsymbol{y}_{t}^{*}|\boldsymbol{y}_{t+1}^{*}) = \frac{1}{\left(\sqrt{2\pi\sigma_{t+1}^{2}}\right)^{d}} \exp\left(-\frac{1}{2\sigma_{t}^{2}} \left\|\sqrt{\frac{\alpha_{t}}{\alpha_{t+1}}}(\boldsymbol{y}_{t+1}^{*} - \frac{\beta_{t+1}}{\sqrt{1-\bar{\alpha}_{t+1}}}\boldsymbol{\epsilon}_{t+1}^{*}) + \sigma_{t+1}\boldsymbol{\epsilon}_{t}^{*}\right) - \sqrt{\frac{\alpha_{t}}{\alpha_{t+1}}}(\boldsymbol{y}_{t+1}^{*} - \frac{\beta_{t+1}}{\sqrt{1-\bar{\alpha}_{t+1}}}\boldsymbol{\epsilon}_{\theta}(\boldsymbol{y}_{t+1}^{*}, t+1)) \right\|_{2}^{2}\right)$$

$$= \frac{1}{\left(\sqrt{2\pi\sigma_{t+1}^{2}}\right)^{d}} \exp\left(-\frac{1}{2\sigma_{t+1}^{2}}\frac{\alpha_{t}}{\alpha_{t+1}}\frac{\beta_{t+1}^{2}}{1-\bar{\alpha}_{t+1}} \left\|\boldsymbol{\epsilon}_{\theta}(\boldsymbol{y}_{t+1}^{*}, t+1) - \boldsymbol{\epsilon}_{t+1}^{*} + \sigma_{t+1}\boldsymbol{\epsilon}_{t}^{*}\right\|_{2}^{2}\right)$$

$$= \frac{1}{\left(\sqrt{2\pi\sigma_{t+1}^{2}}\right)^{d}} \exp\left(-\frac{1}{2}\frac{1-\bar{\alpha}_{t+1}}{(1-\bar{\alpha}_{t})\beta_{t+1}}\frac{\alpha_{t}}{\alpha_{t+1}}\frac{\beta_{t+1}^{2}}{1-\bar{\alpha}_{t+1}} \left\|\boldsymbol{\epsilon}_{\theta}(\boldsymbol{y}_{t+1}^{*}, t+1) - \boldsymbol{\epsilon}_{t+1}^{*} + \sigma_{t+1}\boldsymbol{\epsilon}_{t}^{*}\right\|_{2}^{2}\right)$$

$$= \frac{1}{\left(\sqrt{2\pi\sigma_{t+1}^{2}}\right)^{d}} \exp\left(-\frac{1}{2}\frac{\beta_{t+1}}{(1-\bar{\alpha}_{t})}\frac{\alpha_{t}}{\alpha_{t+1}} \left\|\boldsymbol{\epsilon}_{\theta}(\boldsymbol{y}_{t+1}^{*}, t+1) - \boldsymbol{\epsilon}_{t+1}^{*} + \sigma_{t+1}\boldsymbol{\epsilon}_{t}^{*}\right\|_{2}^{2}\right)$$

The log probability is simply:

$$\log \pi_{\theta}(\boldsymbol{y}_{t}^{*}|\boldsymbol{y}_{t+1}^{*}) = -\frac{1}{2} \frac{\beta_{t+1}\alpha_{t}}{(1-\bar{\alpha}_{t})\alpha_{t+1}} \left\| \boldsymbol{\epsilon}_{\theta}(\boldsymbol{y}_{t+1}^{*}, t+1) - \boldsymbol{\epsilon}_{t+1}^{*} + \sigma_{t+1}\boldsymbol{\epsilon}_{t}^{*} \right\|_{2}^{2}$$
$$-\frac{d}{2} \cdot \log 2\pi - d \cdot \log \sigma_{t+1}$$
(11)

Plugging (11) into (10) yields:

$$\begin{split} \tilde{\mathcal{L}}(\theta) &= -\mathbb{E}\left[\omega_{i,j}\log\sigma\left(-\beta\left[\log\frac{\pi_{\theta}(\boldsymbol{y}_{t,i}^{w}|\boldsymbol{y}_{t+1,i}^{w})}{\pi_{\text{ref}}(\boldsymbol{y}_{t,i}^{w}|\boldsymbol{y}_{t+1,i}^{w})} - \log\frac{\pi_{\theta}(\boldsymbol{y}_{t,j}^{l}|\boldsymbol{y}_{t+1,j}^{l})}{\pi_{\text{ref}}(\boldsymbol{y}_{t,i}^{l}|\boldsymbol{y}_{t+1,i}^{w})}\right]\right)\right] \\ &= -\mathbb{E}\left[\omega_{i,j}\log\sigma\left(-\beta\left[\log\pi_{\theta}(\boldsymbol{y}_{t,i}^{w}|\boldsymbol{y}_{t+1,i}^{w}) - \log\pi_{\text{ref}}(\boldsymbol{y}_{t,i}^{w}|\boldsymbol{y}_{t+1,i}^{w}) - \left(\log\pi_{\theta}(\boldsymbol{y}_{t,j}^{l}|\boldsymbol{y}_{t+1,j}^{l}) - \log\pi_{\text{ref}}(\boldsymbol{y}_{t,j}^{l}|\boldsymbol{y}_{t+1,j}^{l})\right)\right]\right)\right] \\ &= -\mathbb{E}\left[\log\sigma\left(-\beta\frac{\beta_{t+1}\alpha_{t}}{2(1-\bar{\alpha}_{t})\alpha_{t+1}}(\left\|\boldsymbol{\epsilon}_{\theta}(\boldsymbol{y}_{t+1,i}^{w},t) - \boldsymbol{\epsilon}_{t+1}^{w} + \sigma_{t+1}\boldsymbol{\epsilon}_{t}^{w}\right\|_{2}^{2} - \left\|\boldsymbol{\epsilon}_{\text{ref}}(\boldsymbol{y}_{t+1,i}^{w},t) - \boldsymbol{\epsilon}_{t+1}^{w} + \sigma_{t+1}\boldsymbol{\epsilon}_{t}^{w}\right\|_{2}^{2}\right. \\ &\left. - \left(\left\|\boldsymbol{\epsilon}_{\theta}(\boldsymbol{y}_{t+1,j}^{l},t) - \boldsymbol{\epsilon}_{t+1}^{l} + \sigma_{t+1}\boldsymbol{\epsilon}_{t}^{l}\right\|_{2}^{2} - \left\|\boldsymbol{\epsilon}_{\text{ref}}(\boldsymbol{y}_{t+1,j}^{l},t) - \boldsymbol{\epsilon}_{t+1}^{l} + \sigma_{t+1}\boldsymbol{\epsilon}_{t}^{l}\right\|_{2}^{2}\right)\right)\right] \end{split}$$

Similarly, if we approximate y_t^* with the mean of $q(y_t^* | y_{t+1}^*, y_0^*)$, the policy is evaluated as:

$$\begin{split} \pi_{\theta}(\mathbb{E}\left[\boldsymbol{y}_{t}^{*}\mid\boldsymbol{y}_{t+1}^{*},\boldsymbol{y}_{0}^{*}\right]|\boldsymbol{y}_{t+1}^{*}) &= \frac{1}{\left(\sqrt{2\pi\sigma_{t+1}^{2}}\right)^{d}}\exp\left(-\frac{1}{2\sigma_{t}^{2}}\left\|\sqrt{\frac{\alpha_{t}}{\alpha_{t+1}}}(\boldsymbol{y}_{t+1}^{*} - \frac{\beta_{t+1}}{\sqrt{1-\bar{\alpha}_{t+1}}}\boldsymbol{\epsilon}_{t+1}^{*})\right. \\ &- \sqrt{\frac{\alpha_{t}}{\alpha_{t+1}}}(\boldsymbol{y}_{t+1}^{*} - \frac{\beta_{t+1}}{\sqrt{1-\bar{\alpha}_{t+1}}}\boldsymbol{\epsilon}_{\theta}(\boldsymbol{y}_{t+1}^{*},t+1))\right\|_{2}^{2}\right) \\ &= \frac{1}{\left(\sqrt{2\pi\sigma_{t+1}^{2}}\right)^{d}}\exp\left(-\frac{1}{2\sigma_{t+1}^{2}}\frac{\alpha_{t}}{\alpha_{t+1}}\frac{\beta_{t+1}^{2}}{1-\bar{\alpha}_{t+1}}\left\|\boldsymbol{\epsilon}_{\theta}(\boldsymbol{y}_{t+1}^{*},t+1) - \boldsymbol{\epsilon}_{t+1}^{*}\right\|_{2}^{2}\right) \\ &= \frac{1}{\left(\sqrt{2\pi\sigma_{t+1}^{2}}\right)^{d}}\exp\left(-\frac{1}{2}\frac{1-\bar{\alpha}_{t+1}}{(1-\bar{\alpha}_{t})\beta_{t+1}}\frac{\alpha_{t}}{\alpha_{t+1}}\frac{\beta_{t+1}^{2}}{1-\bar{\alpha}_{t+1}}\left\|\boldsymbol{\epsilon}_{\theta}(\boldsymbol{y}_{t+1}^{*},t+1) - \boldsymbol{\epsilon}_{t+1}^{*}\right\|_{2}^{2}\right) \\ &= \frac{1}{\left(\sqrt{2\pi\sigma_{t+1}^{2}}\right)^{d}}\exp\left(-\frac{1}{2}\frac{\beta_{t+1}}{(1-\bar{\alpha}_{t})}\frac{\alpha_{t}}{\alpha_{t+1}}\left\|\boldsymbol{\epsilon}_{\theta}(\boldsymbol{y}_{t+1}^{*},t+1) - \boldsymbol{\epsilon}_{t+1}^{*}\right\|_{2}^{2}\right) \end{split}$$

Again, the log probability is:

$$\log \pi_{\theta}(\mathbb{E}\left[\boldsymbol{y}_{t}^{*} \mid \boldsymbol{y}_{t+1}^{*}, \boldsymbol{y}_{0}^{*}\right] | \boldsymbol{y}_{t+1}^{*}) = -\frac{1}{2} \frac{\beta_{t+1} \alpha_{t}}{(1 - \bar{\alpha}_{t}) \alpha_{t+1}} \left\| \boldsymbol{\epsilon}_{\theta}(\boldsymbol{y}_{t+1}^{*}, t+1) - \boldsymbol{\epsilon}_{t+1}^{*} \right\|_{2}^{2} - \frac{d}{2} \cdot \log 2\pi - d \cdot \log \sigma_{t+1}$$

$$(12)$$

Plugging (12) to (10) yields:

$$\begin{split} \hat{\mathcal{L}}(\theta) &= -\mathbb{E}\left[\omega_{i,j}\log\sigma\left(-\beta\left[\log\frac{\pi_{\theta}(\mathbb{E}\left[\boldsymbol{y}_{t,i}^{w}\mid\boldsymbol{y}_{t+1,i}^{w},\boldsymbol{y}_{0,i}^{w}\right]|\boldsymbol{y}_{t,i}^{w})}{\pi_{\mathrm{ref}}(\mathbb{E}\left[\boldsymbol{y}_{t,i}^{w}\mid\boldsymbol{y}_{t+1,i}^{w},\boldsymbol{y}_{0,i}^{w}\right]|\boldsymbol{y}_{t+1,i}^{w})} - \log\frac{\pi_{\theta}(\mathbb{E}\left[\boldsymbol{y}_{t+1,j}^{l}\mid\boldsymbol{y}_{t+1,j}^{l},\boldsymbol{y}_{0,j}^{l}\right]|\boldsymbol{y}_{t+1,j}^{l})}{\pi_{\mathrm{ref}}(\mathbb{E}\left[\boldsymbol{y}_{t}^{l}\mid\boldsymbol{y}_{t+1,i}^{l},\boldsymbol{y}_{0,i}^{w}\right]|\boldsymbol{y}_{t+1,i}^{w})} - \log\frac{\pi_{\theta}(\mathbb{E}\left[\boldsymbol{y}_{t}^{l}\mid\boldsymbol{y}_{t+1,j}^{l},\boldsymbol{y}_{0,j}^{l}\right]|\boldsymbol{y}_{t+1,j}^{l})}{\pi_{\mathrm{ref}}(\mathbb{E}\left[\boldsymbol{y}_{t}^{w}\mid\boldsymbol{y}_{t+1,i}^{w},\boldsymbol{y}_{0,i}^{w}\right]|\boldsymbol{y}_{t+1,j}^{w})} - \log\pi_{\mathrm{ref}}(\mathbb{E}\left[\boldsymbol{y}_{t}^{w}\mid\boldsymbol{y}_{t+1,i}^{w},\boldsymbol{y}_{0,i}^{w}\right]|\boldsymbol{y}_{t+1,j}^{w})} - \log\pi_{\mathrm{ref}}(\mathbb{E}\left[\boldsymbol{y}_{t}^{w}\mid\boldsymbol{y}_{t+1,i}^{w},\boldsymbol{y}_{0,i}^{w}\right]|\boldsymbol{y}_{t+1,i}^{w}) - \log\pi_{\mathrm{ref}}(\mathbb{E}\left[\boldsymbol{y}_{t}^{l}\mid\boldsymbol{y}_{t+1,j}^{l},\boldsymbol{y}_{0,j}^{l}\right]|\boldsymbol{y}_{t+1,i}^{l})) \right] \right] \\ &= -\mathbb{E}\left[\log\sigma\left(-\beta\frac{\beta_{t+1}\alpha_{t}}{2(1-\bar{\alpha}_{t})\alpha_{t+1}}(\|\boldsymbol{\epsilon}_{\theta}(\boldsymbol{y}_{t+1,i}^{w},t+1)-\boldsymbol{\epsilon}_{t+1}^{w}\|_{2}^{2}-\|\boldsymbol{\epsilon}_{\mathrm{ref}}(\boldsymbol{y}_{t+1,i}^{w},t+1)-\boldsymbol{\epsilon}_{t+1}^{w}\|_{2}^{2}) - \|\boldsymbol{\epsilon}_{\mathrm{ref}}(\boldsymbol{y}_{t+1,i}^{l},t+1)-\boldsymbol{\epsilon}_{t+1}^{l}\|_{2}^{2})\right)\right] \\ &-(\|\boldsymbol{\epsilon}_{\theta}(\boldsymbol{y}_{t+1,j}^{l},t+1)-\boldsymbol{\epsilon}_{t+1}^{l}\|_{2}^{2}-\|\boldsymbol{\epsilon}_{\mathrm{ref}}(\boldsymbol{y}_{t+1,j}^{l},t+1)-\boldsymbol{\epsilon}_{t+1}^{l}\|_{2}^{2}))\right] \end{aligned}$$

B Related Works

B.1 Diffusion Based Text-to-Image Models

Diffusion models [Ho et al., 2020, Sohl-Dickstein et al., 2015, Song et al., 2020, Dhariwal and Nichol, 2021] have been the state-of-the-art in image generation. A diffusion model consists of a forward process that gradually adds noise to the image and attempts to learn to reverse this process with a neural network. Diffusion-based T2I models have also achieved impressive results in producing high-quality images that closely adhere to the given caption [Nichol et al., 2022, ram, 2022, Rombach et al., 2022b, Saharia et al., 2022, Podell et al., 2023a]. However, these models are pre-trained on large web dataset and may not align with human preference. Our work aims to tackle this issue by improving T2I model alignment using semantically related prompt-image pairs

B.2 Diffusion-DPO

Diffusion-DPO [Wallace et al., 2024] generalizes the efficient DPO [Rafailov et al., 2023] to diffusion model alignment. Diffusion-DPO defines reward $R(x, y_{0:T})$ on the diffusion path for prompt x, latents $y_{1:T}$ and image y_0 . The RLHF loss is defined as:

$$\max_{\boldsymbol{v}} \mathbb{E}_{\boldsymbol{x} \sim \mathcal{D}_{x}, \boldsymbol{y}_{0:T} \sim p_{\theta}(\boldsymbol{y}_{0:T} \mid \boldsymbol{x})} \left[r\left(\boldsymbol{x}, \boldsymbol{y}_{0}\right) \right] - \beta \mathbb{D}_{\mathrm{KL}} \left[p_{\theta}\left(\boldsymbol{y}_{0:T} \mid \boldsymbol{x}\right) \| p_{\mathrm{ref}}\left(\boldsymbol{y}_{0:T} \mid \boldsymbol{x}\right) \right]$$
(13)

where $r(\boldsymbol{x}, \boldsymbol{y}_0) = \mathbb{E}_{p_{\theta}(\boldsymbol{y}_{1:T}|\boldsymbol{y}_0, \boldsymbol{x})}[R(\boldsymbol{x}, \boldsymbol{y}_{0:T})]$ is the marginalized image reward across all possible diffusion trajectories.

With some approximation and algebra, the Diffusion-DPO loss can be simplified to:

$$L(\theta) = -\mathbb{E}_{\left(\boldsymbol{y}_{0}^{w}, \boldsymbol{y}_{0}^{l}\right) \sim \mathcal{D}, t \sim \mathcal{U}(0, T),} \log \sigma \left(-\beta T \omega \left(\lambda_{t}\right) \left(\left\|\boldsymbol{\epsilon}^{w} - \boldsymbol{\epsilon}_{\theta} \left(\boldsymbol{y}_{t}^{w}, t\right)\right\|_{2}^{2} - \left\|\boldsymbol{\epsilon}^{w} - \boldsymbol{\epsilon}_{\text{ref}} \left(\boldsymbol{y}_{t}^{w}, t\right)\right\|_{2}^{2} \right.$$

$$\left. \boldsymbol{y}_{t}^{l} \sim q\left(\boldsymbol{y}_{t}^{w} | \boldsymbol{y}_{0}^{w}\right), \\ \left. \boldsymbol{y}_{t}^{l} \sim q\left(\boldsymbol{y}_{t}^{l} | \boldsymbol{y}_{0}^{l}\right)\right) - \left(\left\|\boldsymbol{\epsilon}^{l} - \boldsymbol{\epsilon}_{\theta} \left(\boldsymbol{y}_{t}^{l}, t\right)\right\|_{2}^{2} - \left\|\boldsymbol{\epsilon}^{l} - \boldsymbol{\epsilon}_{\text{ref}} \left(\boldsymbol{y}_{t}^{l}, t\right)\right\|_{2}^{2}\right)\right)$$

$$\left. (14)$$

The approximate Diffusion-RPO loss is a function of denoising diffusion loss, which is simple to compute. However, it is limited to the prompt-image pairs that shares identical prompts.

B.3 Relative Preference Optimization

Relative Preference Optimization [Yin et al., 2024] (RPO) draws inspiration from human cognition that often involves interpreting divergent responses, not only to identical questions but also to those that are similar.

RPO utilizes both identical and semantically related prompt-response pairs in a batch and weight them by the similarity of the prompts between preferred and rejected data. Assume we have unpaired data with N preferred prompt-response pairs and M rejected prompt-response pairs, $(y_{w,i}, x_i)$, $(y_{l,j}, x_j)$, $i \in [N]$, $j \in [M]$ The RPO loss function is given by:

$$\mathcal{L}_{RPO} = -\frac{1}{M*N} \sum_{i=1}^{M} \sum_{j=1}^{N} \log \sigma \left(\omega_{ij} \times \beta \left(\log \frac{\pi_{\theta} \left(y_{w,i} \mid x_i \right)}{\pi_{ref} \left(y_{w,i} \mid x_i \right)} - \log \frac{\pi_{\theta} \left(y_{l,j} \mid x_j \right)}{\pi_{ref} \left(y_{l,j} \mid x_j \right)} \right) \right)$$
(15)

where

$$\omega_{ij} = \frac{\tilde{\omega}_{ij}}{\sum_{i'=1}^{N} \tilde{\omega}_{ij'}}, \quad \tilde{\omega}_{ij} = \exp\left(-\frac{\cos\left(f\left(x_{w,i}\right), f\left(x_{l,j}\right)\right)}{\tau}\right)$$

where $f(\cdot)$ is a text encoder, and τ is the temperature parameter. Intuitively, RPO constructs a correlation matrix of prompts within the mini-batch and normalizes the weights across each column to incorporate semantically related prompts into preference optimization.

RPO significantly improves the alignment of LLMs with human preferences by better emulating the human learning process through innovative contrastive learning strategies.

C Odds Ratio Relative Preference Optimization

Recent work on Odds Ratio Preference optimization (ORPO) [Hong et al., 2024] developed a one-stage preference tuning algorithms for LLMs that combines a SFT term and an odds ratio term in the loss function:

$$\mathcal{L}_{ORPO} = \mathbb{E}_{(\boldsymbol{x}, \boldsymbol{y}^{w}, \boldsymbol{y}^{l})} \left[\mathcal{L}_{SFT} - \lambda \cdot \log \sigma \left(\log \frac{\mathbf{odds}_{\theta} \left(\mathbf{y}^{\mathbf{w}} \mid \mathbf{x} \right)}{\mathbf{odds}_{\theta} \left(\mathbf{y}^{l} \mid \mathbf{x} \right)} \right) \right]$$
(16)

where $\mathbf{odds}_{\theta}(\mathbf{y} \mid \mathbf{x}) = \frac{\pi_{\theta}(\mathbf{y} \mid \mathbf{x})}{1 - \pi_{\theta}(\mathbf{y} \mid \mathbf{x})}$.

ORPO has two major advantages: (1) It does not require an SFT warm-up when there is a domain gap between the downstream task and the pre-training data. (2) It does not require a reference model in the preference learning term.

It is natural to extend ORPO to image preference learning, though such attempts has been made by HuggingFace ². The implementation in this code base uses a coarse approximation to log-probability with the denoising Mean Squared Error in DDPM [Ho et al., 2020].

We proposed a Diffusion Odds Ratio Relative Preference Optimization(ORRPO) loss using our techniques for deriving the RPO loss. For timestep t, we again sample $\boldsymbol{y}_{t+1,\cdot}^*$ from the forward diffusion process and approximate $\boldsymbol{y}_{t,\cdot}^*$ with its posterior mean. the Diffusion-ORRPO loss at time step t can be written as:

 $^{^2} https://github.com/huggingface/diffusers/tree/main/examples/research_projects/diffusion_orpolects/dif$

$$\mathcal{L}_{\text{ORRPO},t}(\theta) = -\|\boldsymbol{\epsilon}_{t+1,i}^{w} - \boldsymbol{\epsilon}_{\theta} \left(\boldsymbol{y}_{t+1,i}^{w}, t+1, i \right) \|_{2}^{2} - \omega_{i,j} \lambda \log \sigma \left(\log \frac{\pi_{\theta}(\boldsymbol{y}_{t+1,i}^{w} | \boldsymbol{y}_{t,i}^{w})}{(1 - \pi_{\theta}(\boldsymbol{y}_{t+1,i}^{w} | \boldsymbol{y}_{t,i}^{w}))} - \log \frac{\pi_{\theta}(\boldsymbol{y}_{t+1,j}^{l} | \boldsymbol{y}_{t,j}^{l})}{(1 - \pi_{\theta}(\boldsymbol{y}_{t+1,i}^{l} | \boldsymbol{y}_{t,i}^{w}))} \right)$$

$$= -\|\boldsymbol{\epsilon}_{t+1}^{w} - \boldsymbol{\epsilon}_{\theta} \left(\boldsymbol{y}_{t+1,i}^{w}, t+1 \right) \|_{2}^{2} - \omega_{i,j} \lambda \log \left(\|\boldsymbol{\epsilon}_{t+1}^{w} - \boldsymbol{\epsilon}_{\theta} \left(\boldsymbol{y}_{t+1,i}^{w}, t+1 \right) \|_{2}^{2} - \|\boldsymbol{\epsilon}_{t+1}^{l} - \boldsymbol{\epsilon}_{\theta} \left(\boldsymbol{y}_{t+1,j}^{l}, t+1 \right) \|_{2}^{2} \right) \right)$$

$$- \left[\log(1 - \pi_{\theta}(\boldsymbol{y}_{t,i}^{w} | \boldsymbol{y}_{t+1,i}^{w})) - \log(1 - \pi_{\theta}(\boldsymbol{y}_{t,j}^{l} | \boldsymbol{y}_{t+1,j}^{l})) \right] \right)$$

$$\approx -\|\boldsymbol{\epsilon}_{t+1}^{w} - \boldsymbol{\epsilon}_{\theta} \left(\boldsymbol{y}_{t+1,i}^{w}, t+1 \right) \|_{2}^{2} - \omega_{i,j} \lambda \log \sigma \left(\|\boldsymbol{\epsilon}_{t+1}^{w} - \boldsymbol{\epsilon}_{\theta} \left(\boldsymbol{y}_{t+1,i}^{w}, t+1 \right) \|_{2}^{2} - \|\boldsymbol{\epsilon}_{t+1}^{l} - \boldsymbol{\epsilon}_{\theta} \left(\boldsymbol{y}_{t+1,j}^{l}, t+1 \right) \|_{2}^{2} \right) \right)$$

$$- \left[\log(1 - \exp\left(\frac{1}{2} \|\boldsymbol{\epsilon}_{t+1}^{w} - \boldsymbol{\epsilon}_{\theta} \left(\boldsymbol{y}_{t+1,i}^{w}, t+1 \right) \|_{2}^{2} \right) - \log(1 - \exp\left(\frac{1}{2} \|\boldsymbol{\epsilon}_{t+1}^{l} - \boldsymbol{\epsilon}_{\theta} \left(\boldsymbol{y}_{t+1,j}^{l}, t+1 \right) \|_{2}^{2} \right) \right) \right] \right)$$

Here we approximate Gaussian density with $\exp\left(\frac{1}{2}\|\boldsymbol{\epsilon}_{t+1}^* - \boldsymbol{\epsilon}_{\theta}\left(\boldsymbol{y}_{t+1,k}^*, t+1\right)\|_2^2\right)$ for simplicity. Let $\text{MSE}_{t+1,k}^*\left(\theta\right) := \|\boldsymbol{\epsilon}_{t+1}^* - \boldsymbol{\epsilon}_{\theta}\left(\boldsymbol{y}_{t+1,k}^*, t+1\right)\|_2^2$, our Diffusion-ORRPO loss can be written as

$$\mathcal{L}_{\mathrm{ORRPO}}(\theta) = \mathbb{E}\left[-\mathrm{MSE}_{t+1,i}^{w}\left(\theta\right) - \omega_{i,j}\lambda\log\sigma\left(\mathrm{MSE}_{t+1,i}^{w}\left(\theta\right) - \mathrm{MSE}_{t+1,j}^{l}\left(\theta\right) - \left[\log(1-\exp\left(-\frac{1}{2}\mathrm{MSE}_{t+1,i}^{w}\left(\theta\right)\right)\right)\right]\right)\right]$$

$$\log(1-\exp\left(-\frac{1}{2}\mathrm{MSE}_{t+1,j}^{l}\left(\theta\right)\right))\right]$$

where the expectation is taken over timesteps and preference pairs, the re-weighting term $\omega_{i,j}$ is the same as Diffusion-RPO.

Our preliminary experiment with $ORRPO(\lambda=0.2, \tau=0.01)$ on SDXL achieves 28.660 HPSV2 score and 22.827 Pick score on HPSV2 test set, which is higher than the best ORPO ($\lambda=0.005$) result with 28.084 HPSV2 score and 22.037 Pick score. However, neither Diffusion-ORPO nor Diffusion-ORPO is able to bridge the domain gap in style alignment tasks without the SFT warmup and reference models. We observe in our experiment that although Diffusion-ORPO and Diffusion-ORPO can correctly produce style-aligned images for some prompts, they fail on others. This observation underscores the intrinsic difficulty of efficiently fine-tuning diffusion based T2I models under strong distribution shift. We leave further investigation of this issue to future work.

D Win Rates Evaluation

We report the win rate between RPO generation v.s. baselines in Table 4. To ensure the robustness of evaluataion. We generate 5 images per prompt for the two competing models and compare the median reward model score.

Table 4: Win rates for RPO v.s. existing alignment approaches under various reward models using prompts from the HPSV2 and Parti-Prompt datasets. On SD1.5, the temperature parameter is chosen to be 0.01, on SD1.5 and 0.5 on SDXL

Model	Test Dataset	Method	HPS	Pick Score	Aesthetics	CLIP	Image Reward
SD1.5	HPSV2	RPO (ours) v.s. Base	74.84	74.81	68.38	59.53	66.88
		RPO (ours) v.s. SFT	51.91	32.22	44.0	50.69	39.28
		RPO (ours) v.s. DPO [Wallace et al., 2024]	59.63	52.78	53.13	49.63	54.25
SD1.5		RPO (ours) v.s. Base	66.24	64.28	64.71	57.84	60.72
	Parti-Prompt	RPO (ours) v.s. SFT	52.39	33.58	40.63	53.49	43.44
		RPO (ours) v.s. DPO [Wallace et al., 2024]	56.68	50.98	52.94	48.96	54.60
SDXL	HPSV2	RPO (ours) v.s. Base	93.09	83.59	50.59	65.28	79.41
		RPO (ours) v.s. SFT	79.53	95.94	81.13	62.59	78.84
		RPO (ours) v.s. DPO [Wallace et al., 2024]	64.28	57.16	51.44	49.63	57.41
		RPO (ours) v.s. Base	90.63	79.60	65.07	62.75	82.23
	Parti-Prompt	RPO (ours) v.s. SFT	79.78	95.10	79.41	67.40	81.00
		RPO (ours) v.s. DPO [Wallace et al., 2024]	64.09	$\boldsymbol{58.52}$	59.80	48.35	58.58

E Additional Details:

We used $\beta=5000$ for all experiments. Following Wallace et al. [2024], we use AdamW for SD 1.5 [Loshchilov and Hutter, 2019] and AdaFactor for SDXL [Shazeer and Stern, 2018]. For human preference alignment, we adopted a learning rate of $\frac{2000}{\beta}2.048 \cdot 10^{-8}$. For style alignment, the learning rate is set to be $\frac{2000}{\beta}2.048 \cdot 10^{-8}$ in the first stage. In second stage, we use $\frac{2000}{\beta}2.048 \cdot 10^{-8}$ for Van Gogh and $\frac{2000}{\beta}2.048 \cdot 10^{-9}$ for Sketch and Winter datasets. Eight Nvidia A100 GPUs were used for training. The local batch size on each GPU is 16 with gradient accumulation of 4 steps for SD 1.5. For SDXL, the local batch size is 8 with gradient accumulation of 8 steps.

F SDXL Style Alignment Details

Table 5: Additional details for SDXL style alignment experiments.

	SFT LR	SFT Steps	Second Stage LR	Second Stage Steps
Van Gogh	1e-7	2000	1e-8	1000
Sketch	1e-7	2000	1e-8	500
Winter	1e-7	2000	1e-8	1000

G Prompts and More Human Preference Alignment Examples

We list the prompts used in Figure 1 as follows

- 1. Kyoto Animation stylized anime mixed with tradition Chinese artworks A dragon flying at modern cyberpunk fantasy world. Cinematic Lighting, ethereal light, gorgeous, glamorous, 8k, super detail, gorgeous light and shadow, detailed decoration, detailed lines
- 2. a masterpiece, batgirl/supergirl from dc comic wearing alternate yellow costume, coy and alluring, full body, Kim Jung gi, freedom, soul, digital illustration, comic style, cyberpunk, perfect anatomy, centered, approaching perfection, dynamic, highly detailed, watercolor painting, artstation, concept art, smooth, sharp focus, illustration, art by Carne Griffiths and Wadim Kashin, unique, award winning, masterpiece

- 3. (Pirate ship sailing into a bioluminescence sea with a galaxy in the sky), epic, 4k, ultra,
- 4. In the vast emptiness of the interstellar void, two omnipotent deities from separate dimensions collide. The Creator, wields the power of creation, bringing forth stars and life forms with a wave of their hand. Opposite them stands the Destroyer, a god whose face is a shifting visage of decay and entropy disintegrating celestial bodies and extinguishing stars.
- 5. neon light art, in the dark of night, moonlit seas, clouds, moon, stars, colorful, detailed, 4k, ultra hd, realistic, vivid colors, highly detailed, UHD drawing, pen and ink, perfect composition, beautiful detailed intricate insanely detailed octane render trending on artstation, 8k artistic photography, photorealistic concept art, soft natural volumetric cinematic perfect light
- 6. Lady with floral headdress, blonde hair, blue eyes, seductive attire, garden, sunny day, realistic texture
- 7. a cute little matte low poly isometric Zelda Breath of the wild forest island, waterfalls, mist, lat lighting, soft shadows, trending on artstation, 3d render, monument valley, fez video game
- 8. a psychedelic surrealist painting of a sunflower, surreal, dripping, melting, Salvador Dali, Pablo Piccaso
- 9. Commercial photography, powerful explosion of golden dust, luxury parfum bottle, yellow sunray, studio light, high resolution photography, insanely detailed, fine details, isolated plain, stock photo, professional color grading, 8k octane rendering, golden blury background
- 10. Digital painting of a beautiful young Japanese woman, dancing, kimono is crafted with waves and layers of fabric, creating a sense of movement and depth, fall season, by (random: famous japanese artists), artstation, 8k, extremely detailed, ornate, cinematic lighting, rim lighting,
- 11. giraffe in flowers by artist arne thun, in the style of natalia rak, 8k resolution, vintage aesthetics, wallpaper, animated gifs, naoto hattori, highly realistic
- 12. bright painting of a tree with stars in the sky, in the style of dreamlike fantasy creatures, multilayered dimensions, swirling vortexes, realistic color schemes, dark green and light blue, light-filled landscapes, mystic mechanisms
- 13. Holy male paladin, looking straight at the viewer, serious facial expression, heavenly aura, bokeh, light bloom, bright light background, cinematic lighting, depth of field, concept art, HDR, ultra high-detail, photorealistic, high saturation
- 14. poster of a blue dragon with sunglasses, in the style of orient-inspired, post-apocalyptic surrealism, light orange and red, 32k uhd, chinapunk, meticulous design, detailed costumes
- 15. Double Exposure Human-Nature, trees, flowers, mountain, sunset, nature mind, expressive creative art, surrealistic concept art, ethereal landscape in a cloud of magic coming out the top of a human head, incredible details, high-quality, flawless composition, masterpiece, highly detailed, photorealistic, 8k sharp focus quality surroundings

Additional sample images from RPO-SDXL are presented in Figure 5 and Figure 6.

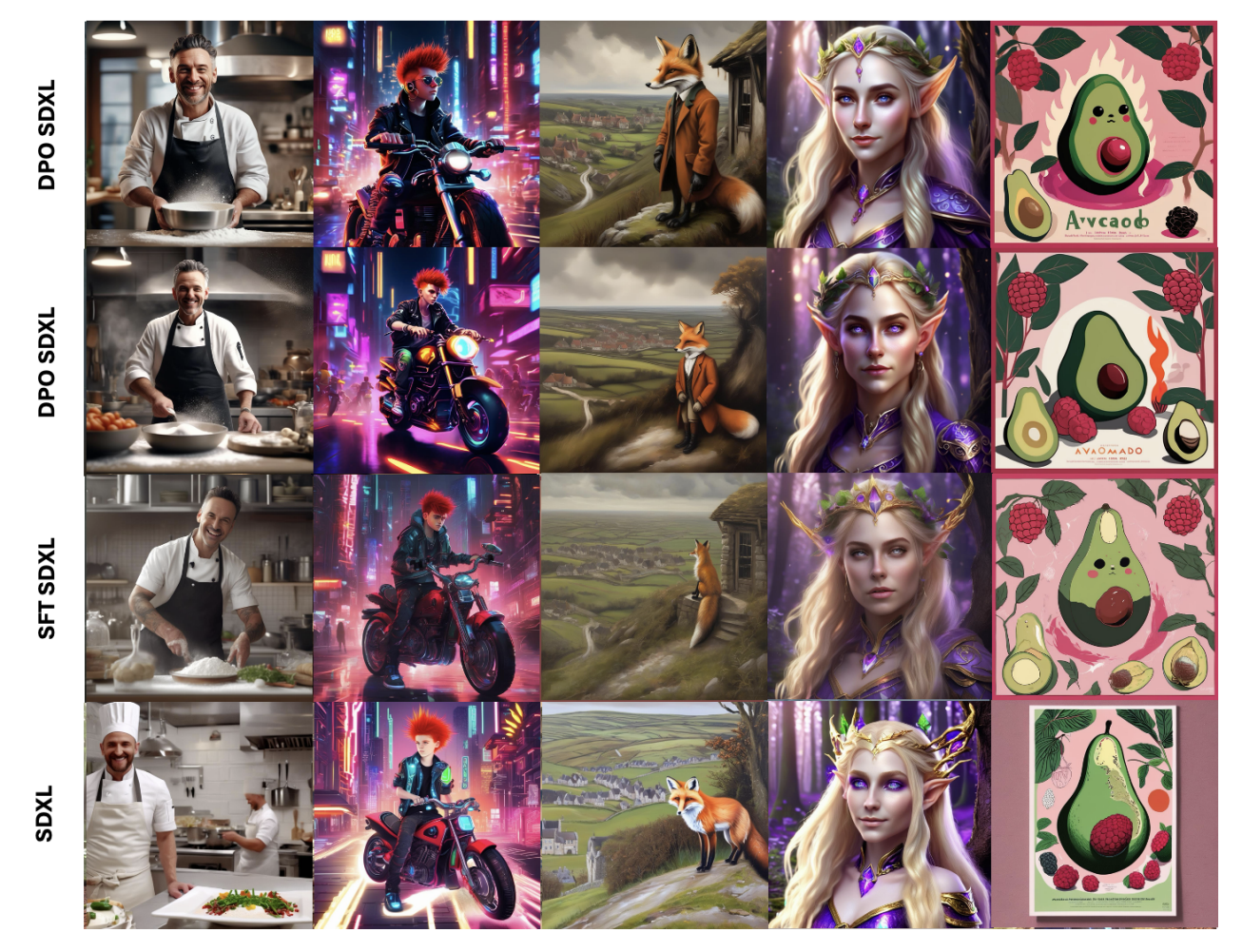


Figure 5: Sample images from RPO-SDXL The prompts used to generate the images are: "A charismatic chef in a bustling kitchen, his apron dusted with flour, smiling as he presents a beautifully prepared dish. 8K, hyper-realistic, cinematic, post-production.", "A rebellious teenage boy with spiked, vibrant red hair, riding a futuristic motorcycle through neon-lit city streets, headphones around his neck blaring electronic music. Best quality, fine details.", "An oil painting of an anthropomorphic fox overlooking a village in the moor.", "A fantasy-themed portrait of a female elf with golden hair and violet eyes, her attire shimmering with iridescent colors, set in an enchanted forest. 8K, best quality, fine details.", "A graphic poster featuring an avocado and raspberry observing a burning world, inspired by old botanical illustrations, Matisse, Caravaggio, Basquiat, and Japanese art."



Figure 6: Sample images from RPO-SDXL The prompts used to generate the images are: "A mysterious priestess in a flowing, ethereal gown, communicating with spirits in a sacred grove, her eyes glowing when she invokes ancient spells. Best quality, fine details.", "A distinguished older gentleman in a vintage study, surrounded by books and dim lighting, his face marked by wisdom and time. 8K, hyper-realistic, cinematic, post-production.", "The image features an ancient Chinese landscape with a mountain, waterfalls, willow trees, and arch bridges set against a blue background.", "A giant dinosaur frozen into a glacier and recently discovered by scientists, cinematic still", "A young male mage with silver hair and mysterious blue eyes, wearing an intricate robe, casting spells with a glowing crystal staff in a dark enchanted forest. Best quality, fine details."

H More Style Alignment Examples

Additional sample images from style-aligned Stable Diffusion models are presented in Figure 7.

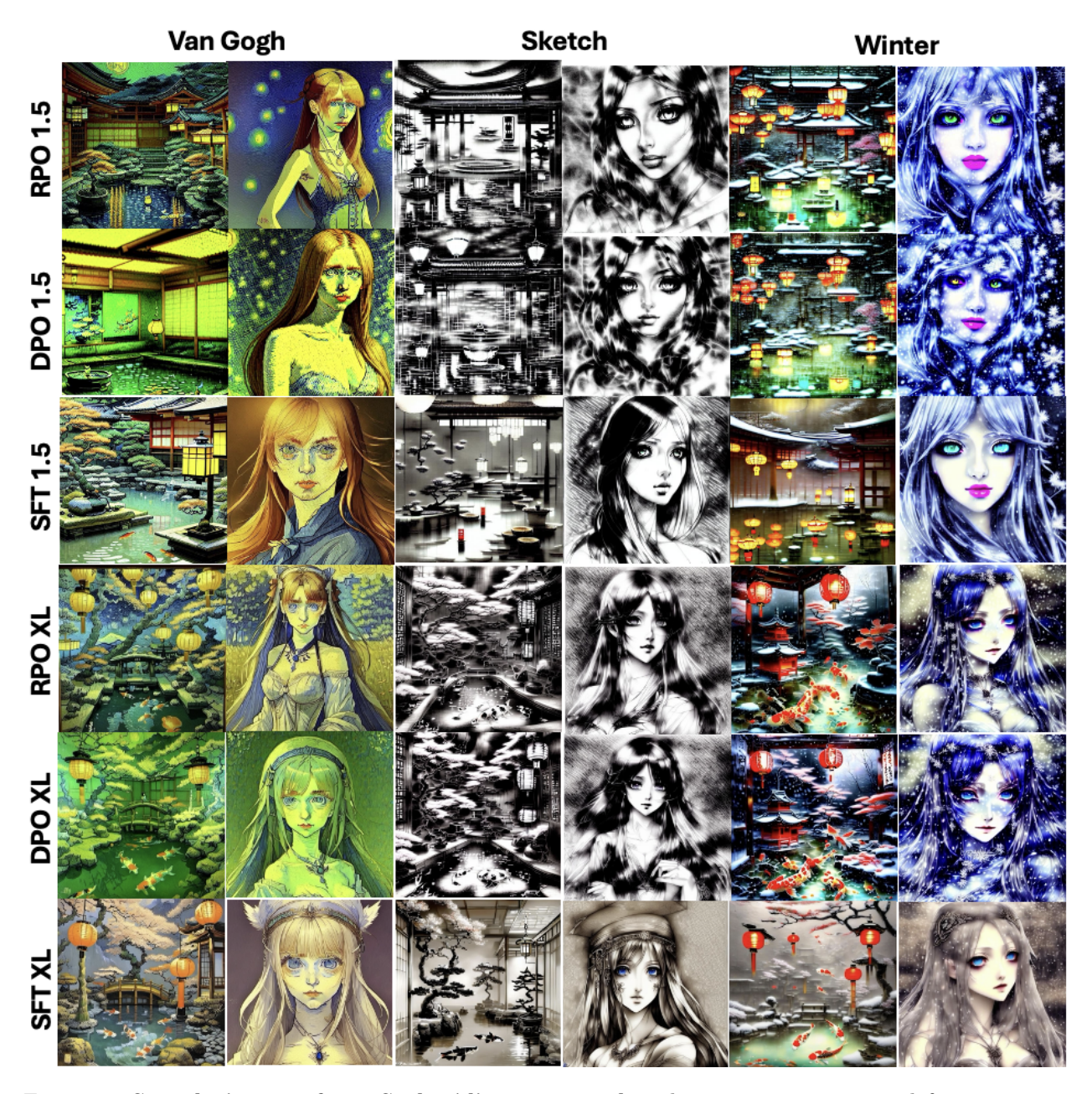


Figure 7: Sample images from Style Alignment Task, the images are generated from prompts: "Japanese hot spring interior with lanterns, koi fish and bonsai trees in a painting by Greg Rutkowski and Craig Mullins.", "A beautiful girl posing dramatically, with stunning eyes and features, by Davinci on Pixiv."

I Social Impacts

Diffusion-RPO enhances the performance of diffusion based T2I models that could democratize artistic creation, allowing individuals without formal training in art to generate high-quality images. This can inspire creativity and make art more accessible. However, there's a risk of these models being used to create misleading images or deepfakes, potentially spreading misinformation or harming individuals' reputations.